Revealing the limits of energy recovery in forward-bias bipolar membranes

Justin C. Bui[1,2*], Eric W. Lees[3], Andrew K. Liu[1,2], Wei Lun Toh[4], Priyamvada Goyal[3], Francisco Javier U. Galang[1,2], Yogesh Surendranath[4], Alexis T. Bell[1,2], and Adam Z. Weber[2,3*]

[1] Department of Chemical and Biomolecular Engineering
University of California Berkeley
Berkeley, CA 94720, USA

[2] Chemical Sciences Division
Lawrence Berkeley National Laboratory
Berkeley, CA 94720, USA

[3] Energy Technologies Area
Lawrence Berkeley National Laboratory
Berkeley, CA 94720, USA

[4] Department of Chemistry
Massachusetts Institute of Technology
Cambridge, MA 02139, USA

Corresponding Authors: justin_bui@berkeley.edu, azweber@lbl.gov
Phone: (571) 269-0395, (510) 486-6308

Abstract

The ability for bipolar membranes (BPMs) to interconvert voltage and pH makes them attractive materials for use in energy conversion and storage. Reverse-biased BPMs, which use electrical voltage to dissociate water into acid and base, have become increasingly well-studied. However, forward-biased BPMs (FB-BPMs), in which voltage is extracted from pH gradients through recombination, are poorly understood. In this work, physics-based modeling elucidates how complex coupling of transport and kinetics dictates the performance of FB-BPMs in electrochemical devices. Simulations reveal that the open-circuit potential (OCP) of FB-BPMs is dictated by the balance of ion recombination and crossover, where recombination of buffering counter-ions attenuates OCP. Uptake of ionic impurities and fixed-charge neutralization limit achievable current densities by reducing the fraction of fixed-charge sites that mediate recombination. The model highlights the importance and nuances of selective ion management in mitigating energy losses and provides insight into the engineering of FB-BPMs for energy applications.
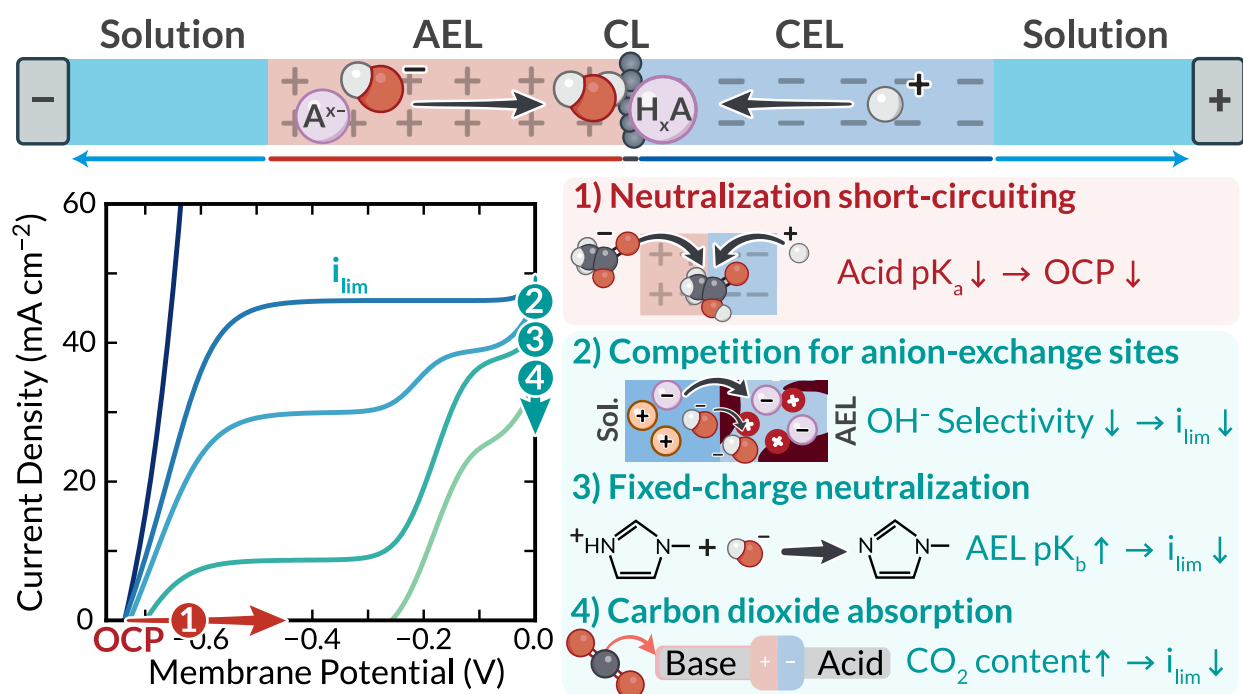
1. Introduction

Bipolar membranes (BPMs) are a class of ion-conducting polymer composites comprised of an anion-exchange layer (AEL) and a cation-exchange layer (CEL), typically with an interfacial catalyst layer (CL) placed in between that accelerates the rate of interfacial dissociation/recombination reactions.[1–3] BPMs possess the ability to convert applied electrical voltage into pH gradients and *vice versa,* thereby creating sustained separate microenvironments on each side, making them useful for a wide variety of applications across the energy and environmental nexus.

BPMs have two operating modes, defined based on the direction of ionic current flow within the BPM.[3] In the reverse-bias (RB) operating mode, the BPM is operated such that counter-ions (*i.e.,* ions with the opposite charge to a given ion-exchange layer) are driven by electro-migration away from the CL. Co-ions (*i.e.,* ions with like charge to a given ion-exchange layer) are impeded from transporting through the BPM by Donnan exclusion. In RB-BPMs, electric-field- and catalytically-enhanced dissociation reactions (*e.g.,* water dissociation (WD)) occur within the CL to ensure current continuity.[4,5] For instance, when using water as the solvent, the voltage applied across the BPM increases the rate of WD, which generates H^+ ions that transport through the CEL, and OH^- that transport through the AEL. This phenomenon effectively transduces applied electrical voltage into a pH gradient. Accordingly, RB-BPMs are employed in environmental applications where sustainably generated acid- and base- are useful (*e.g.,* ammonia separations,[6–8] carbon capture/mineralization[9–11]) or catalytic systems where control of the local pH environment is of value (*e.g.,* water electrolysis,[12,13] CO_2 reduction[14–16]).

While detailed understanding of RB-BPMs has been developed recently, forward-bias (FB)-BPMs are still quite under-explored,[17,18] especially from a theoretical standpoint. In FB, acid and base are fed to the CEL and AEL sides of the BPM, respectively. Co-ions are impeded from leaking through the BPM by Donnan exclusion, maintaining the external pH gradient. This maintenance of disparate chemical environments effectively enables a recovery in voltage wherein the voltage requirements for faradaic reactions at the external electrodes are reduced by the sustained chemical environments. Within the CL, H^+ from the CEL and OH^- from the AEL recombine to form H_2O, which is necessary to facilitate the flow of ionic current.[3,19] The energy savings from FB-BPMs make them attractive for a variety of applications (**Figure 1a**). In CO_2 reduction, FB-BPMs furnish optimal alkaline cathode environments for CO_2 electrolysis, mitigate the crossover of (bi)carbonate species through Donnan exclusion, and reduce energy requirements for electrolysis due to the local electrode environment.[17,20] FB-BPMs also overcome challenges with membrane dehydration in hydrogen fuel cells by generating water as the neutralization product of H^+ and OH^-, which humidifies the cell internally.[21,22] Finally, FB-BPMs can be used to increase the energy density of redox flow batteries (RFBs) by providing additional voltage associated with an applied pH gradient, enabling operation outside the water stability region.[3,23–25]

The polarization curve of a FB-BPM mediating acid-base recombination is shown in **Figure 1b**. These polarization curves are traditionally collected using 4-probe electrochemical cells with linear sweep voltammetry or galvanostatic measurements,[26] and are typically characterized by a sharp increase in current starting from the open-circuit potential (OCP) until a voltage-independent plateau in current density is reached (i_{lim}).[17] The performance of FB-BPMs can be
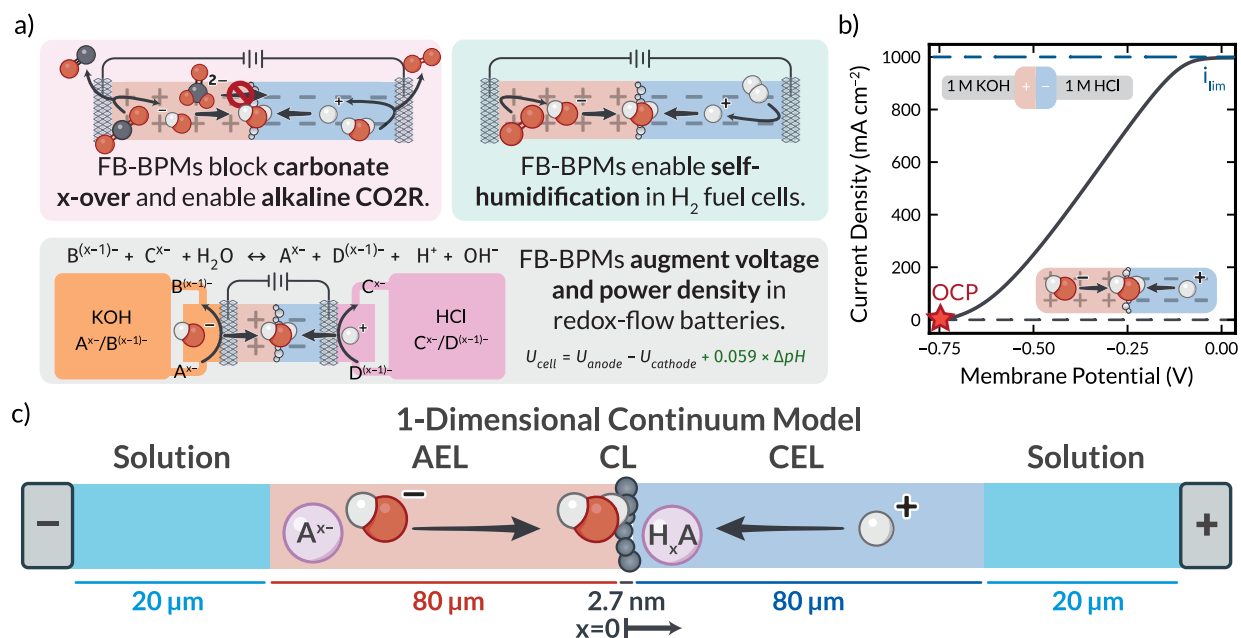
3

Figure 1: *Overview of forward-biased bipolar membranes (FB-BPMs).* **(a)** Use cases for FB-BPMs in energy conversion and storage. **(b)** Polarization behavior for an idealized FB-BPM performing acid-base recombination. This FB-BPM possesses an alkaline 1 M KOH anion-exchange layer (AEL) exchange solution (ES) and an acidic 1 M HCl cation-exchange layer (CEL) exchange solution. The blue dashed line denotes the FB limiting current density, i_{lim}, and the red star denotes the open-circuit potential (OCP). **(c)** Schematic representation of the 1D continuum model used to model FB-BPMs.

characterized by these two values (OCP and i_{lim}). The OCP represents the maximum recoverable voltage from the FB-BPM and is characterized by the Nernstian dependence on the applied pH gradient (*i.e.,* OCP = –0.0591 [V] × ΔpH).[27] i_{lim} represents the maximum achievable rate for acid-base recombination in the catalyst layer, and is controlled by the transport of H^+ and OH^- from the external electrolyte to the AEL|CEL interface.[17] Maximizing both the OCP and i_{lim} is required to attain meaningful current or power densities for energy storage and conversion.

FB-BPMs have yet to achieve industrially relevant current and power densities for applications in energy conversion and storage. New strategies for maximizing and recovering OCP and i_{lim} in FB-BPMs are therefore warranted; however, this effort is made complicated by the various phenomena in FB-BPMs that remain unexplained. For instance, recent experiments by Dinh *et al.* demonstrated that the OCP of a FB-BPM is not proportional to the external pH gradient as suggested by classical thermodynamics,[28] but rather is proportional to the pK_a or pK_b of the dominant weak buffer in the system.[18] These experiments provide evidence for a mechanism wherein parasitic neutralization reactions attenuate recoverable voltage,[18] but a complete understanding of this phenomenon has not yet been established. Additionally, while multiple recent studies have shown that limiting current densities in FB-BPMs are significantly diminished in the presence of counter-ion impurities that compete with H^+ and OH^- for fixed-charge sites in the BPM,[17,29] quantitative agreement with theory across multiple electrolytes concentrations has not been achieved. Hence, the mechanisms behind these losses remains unclarified.[29] A complete

physics-based description involving chemical engineering principles of multi-component transport coupled with kinetics of recombination and thermodynamic repulsion is therefore necessary to quantify energy losses and optimize FB-BPM devices. This is especially true since most FB-BPM devices use electrolytes comprised of weak bases and acids (*e.g.*, bicarbonate (HCO_3^-), formate ($HCOO^-$), or acetate (OAc^-) in CO_2 reduction[30–32]) or contain impurities (*e.g.*, atmospheric absorption of CO_2 in H_2 fuel cells[33]).

Here, we report a continuum, multiphysics model of forward-bias BPMs (**Figure 1c**) that resolves multi-ion transport, Donnan exclusion, and acid/base recombination in various electrolytes relevant to CO_2 electrolysis, H_2 fuel cells, and RFBs. The model couples a modified Poisson-Nernst-Planck transport model with non-equilibrium mass-action-law kinetics to quantify the rates of acid-base recombination at the BPM junction and identify the physical origin of OCPs and limiting current densities in FB-BPMs. The model is validated for various chemical environments and electrolytes relevant to FB-BPM application, including buffers possessing a wide range of pK_as and pK_bs and multiple valences.

Remarkably, a single set of five model parameters pertaining to the membrane properties are sufficient to predict the OCPs and limiting current density of BPMs exchanged with 24 different electrolyte solutions measured experimentally[17,18] (denoted herein as "A | C BPMs" where A is the AEL-exchange-solution and C is the CEL-exchange-solution). The resolved concentration profiles and reaction rates elucidated the dominant phenomena in the FB-BPM polarization curves, and sheds light on the importance of often neglected non-ideal, multi-component phenomena (*e.g.*, CO_2 uptake, fixed-charge neutralization, ion-selective partitioning) in dictating the limits of energy recovery and the role of transport mechanisms. Finally, we examine rational materials design and ion-management strategies to enable substantially improved FB-BPMs power densities for various applications.

2. Results and Discussion

2.1 pK_a and pK_b of weak buffers dictate open-circuit potential in forward-bias bipolar membranes

According to classical equilibrium thermodynamics,[28] the OCP of a FB-BPM should possess a Nernstian dependence on the pH gradient across the system in the absence of the Donnan potentials that dictate voltage loss associated with ion-exchange across a charged interface (**Supplementary Note 8**).

$$OCP = -2.303\frac{RT}{F}(pH_{AEL-ES} - pH_{CEL-ES}), \tag{1}$$

where R is the ideal gas constant, T is the absolute temperature, F is Faraday's constant, pH_{AEL-ES} is the pH of the AEL exchange solution, and pH_{CEL-ES} is the pH of the CEL exchange solution. Throughout this manuscript, negative voltage is voltage that can be recovered in FB, and positive voltage is net voltage applied across the FB-BPM. Positive current density represents current density associated with counter-ion transport towards the BPM junction, and negative current density represents counter-ion transport away from the BPM junction.

Interestingly, recent work by Dinh *et al.* has demonstrated that this dependence breaks down for BPMs exchanged with buffering electrolytes.[18] Instead of the OCP being dictated by the pH

difference across the BPM, it is instead dictated by an approximately Nernstian dependence on the pK_a or pK_b of the buffering ion with which the BPM is exchanged (**Figure 2a-b**). The work of Dinh *et al.* proposes a mechanism for this dependence that was coined "neutralization short-circuiting," in which recombination current from the neutralization of the buffering anion or cation reduces the OCP from its Nernstian (thermodynamic) value.[18] The onset of this depends on the pK_a or pK_b of the recombining buffer via a Nernstain effect,[9] hence explaining the dependence of the OCP on the pK_a or pK_b of the exchanged counter-ion. Notably, the measured OCP of the $K_3PO_4|H_2SO_4$ BPM, where the AEL is exchanged with a trivalent PO_4^{3-} anion, deviated substantially from the observed trend of OCP on buffer pK_a, exhibiting an OCP far lower than what would be expected from a Nernstian dependence on pK_a (**Figure 2a**).

As shown in **Figure 2a-b** (see **Supplementary Figures 4-5** for full simulated polarization data), our simulations accurately predict the OCPs of all 17 1 M K_iA | 1 M H_2SO_4 and 1 M KOH | 1 M BCl BPMs measured experimentally,[18] where A and B are the identities of the buffering anion or cation, respectively, and i represents ion valence, including the peculiar outlier of the K_3PO_4-exchanged BPM. Furthermore, the model enables deconvolution of the ionic processes ensuing within the BPM (see **Figure 2d**). This current-density-breakdown analysis deconstructs the polarization curve, demonstrating how the FB-BPM OCP is governed by current density arising from the neutralization of buffering counter-ions balanced by current density associated with the crossover and dissociation of co-ions (shown schematically in **Figure 2c**). By proving that recombination is the dominant contributor to current density near the OCP, this analysis corroborates the proposed neutralization short-circuiting mechanism established by Dinh *et al.*[18] Moreover, the simulation demonstrates that while OCP is commonly thought of as a static thermodynamic property, OCP in FB-BPMs is dictated by an intricate balance between multiple, dynamic transport and kinetic processes occurring simultaneously in the FB-BPM.

Examining the concentration profiles in a 1 M KOAc | 1 M H_2SO_4 FB-BPM sheds further light on the physical mechanisms that dictate OCP (**Supplementary Figures 6-8**). At potentials more negative than 0.0591 [V] $\times$ $pK_{a,HOAc}$ (the onset of OAc^- and H^+ recombination), OAc^- anions build up at the AEL|CL interface because they are drawn to the AEL|CL interface *via* migration and diffusion but are impeded from entering the CEL by Donnan exclusion. However, once the potential exceeds the onset for OAc^- and H^+ recombination, HOAc is generated at the interface and, due to its neutral nature, can be transported out of either the AEL or CEL by diffusion. Importantly, the transport of neutral HOAc out of the CEL results in a net crossover of OAc^- through the BPM at voltages beyond its recombination onset, consistent with prior studies.[18] These calculated concentration profiles underscore the role of recombination at the AEL|CEL interface in dictating the energetics, crossover, and local microenvironments of FB-BPMs.

As noted above, Dinh *et al.* could not explain the OCP vs. pK_a trend for the 1 M K_3PO_4 | 1 M H_2SO_4 FB-BPM.[18] As shown in **Figure 2a**, the developed theory herein can replicate quite well the experimentally observed outlier. Current-density-breakdown analysis demonstrates that this outlier occurs because the FB-BPM OCP depends not only on the pK_a but also on the valence of the recombining ion. As can be seen in **Figure 2e**, the dominant contribution to current density near the OCP is not the recombination of PO_4^{3-} and H^+, which may be expected due to the prevalence of PO_4^{3-} in the bulk electrolyte, but rather the recombination of HPO_4^{2-} and H^+. In fact, the recombination of PO_4^{3-} and H^+ contributes negligibly throughout the range of tested voltages.
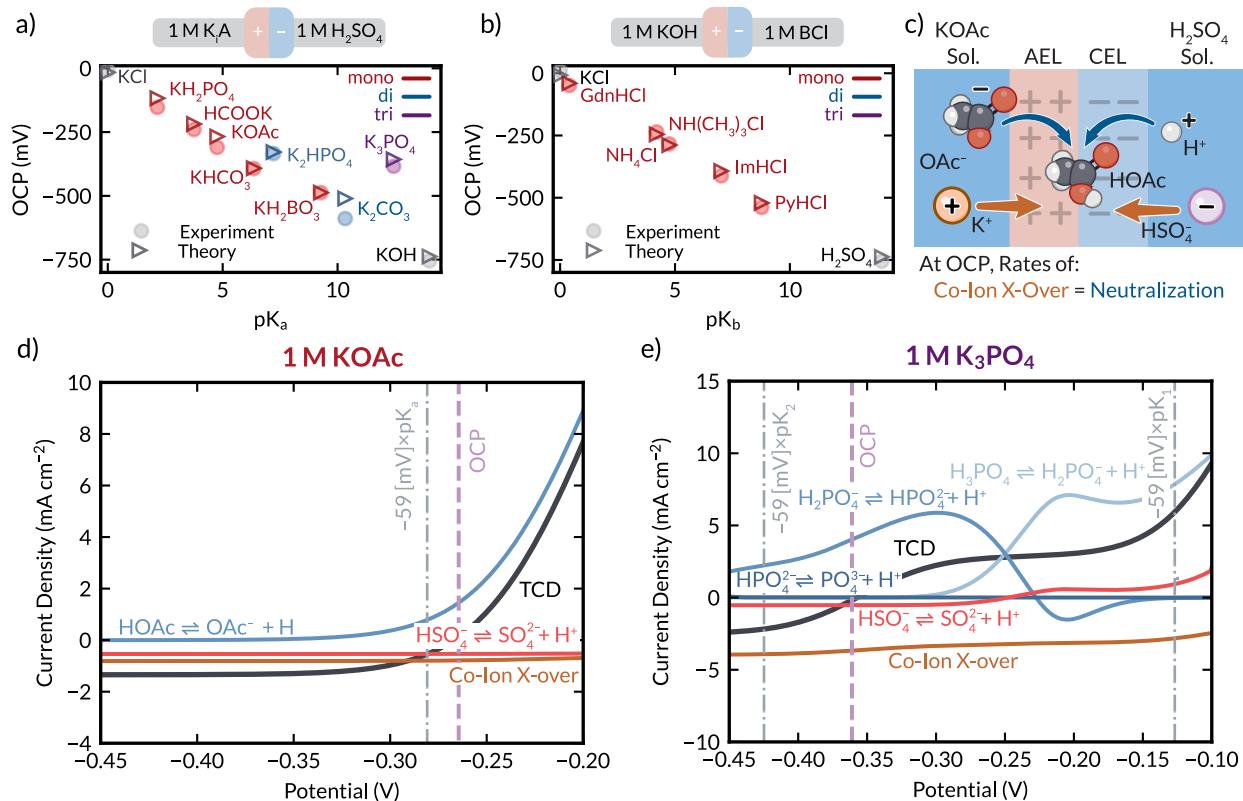
Figure 2: *Theory resolves attenuation of open-circuit potential (OCP) in forward-biased bipolar membranes (FB-BPMs).* **(a)** Comparison of experimental (circular markers) and theoretically calculated (triangular markers) OCP as a function of conjugate acid pK_a, for 1 M K_iA | 1 M H_2SO_4 BPM, where A is the identity of the buffering anion, and i is its valence. Color of the OCP data-point denotes the valence of the buffering anion, with red being used for monovalent anions, blue for divalent anions, and purple for trivalent anions. **(b)** Comparison of experimental (circles) and theoretically calculated (triangles) OCP as a function of conjugate base pK_b, for 1 M KOH | 1 M BCl BPM, where B is the identity of the buffering cation. **(c)** Schematic depiction of the physical processes that dictate OCP in FB-BPMs. **(d)** Current-density breakdown analysis of a 1 M KOAc | 1 M H_2SO_4 BPM. **(e)** Current density breakdown analysis of a 1 M K_3PO_4 | 1 M H_2SO_4 BPM. Experimental data for panels **(a)** and **(b)** are taken from prior work by Dinh *et al.*[18]

This phenomenon is better understood by examining the concentration profiles of the 1 M K_3PO_4 | 1 M H_2SO_4 FB-BPM (**Supplementary Note 9.3**), where incoming PO_4^{3-} clearly speciates into HPO_4^{2-} within the AEL, and the AEL is primarily in its HPO_4^{2-}-form at the AEL|CL interface. Accordingly, the reaction occurring in the CL is the recombination of HPO_4^{2-} and H^+. This finding also explains why the OCP of the 1 M K_3PO_4 | 1 M H_2SO_4 and 1 M K_2HPO_4 | 1 M H_2SO_4 FB-BPMs are so similar: both OCPs are dictated by the same recombination reaction. Accordingly, the valence of a buffering anion dictates its OCP and polarization behavior due to the ability of multivalent anions to speciate internally according to pH gradients within the AEL. Furthermore, theoretical analysis of BPMs exchanged with phosphate anions of varying valence (**Supplementary Note 9**) demonstrates that, beyond the OCP, accounting for internal speciation reactions out of equilibrium facilitates understanding of nontrivial curvature observed in

7

experimental polarization data with multivalent anion electrolytes in both forward and reverse bias (**Supplementary Figure 31**). This analysis underscores the importance of a physical understanding of nonequilibrium behavior in predicting experimentally observed energetics and rates in FB-BPM systems.

2.2 Competition between counter-ions dictates OCP and limiting current density in mixed electrolytes

While the above analysis demonstrates the ability of nonequilibrium continuum theory to predict performance of FB-BPMs where the individual ion-exchange layers are exchanged with electrolytes of a single salt, many systems relevant for energy conversion and environmental remediation necessitate the use of complex, multi-component electrolytes containing weak-buffer impurities (*e.g.,* (bi)carbonate electrolytes in CO_2 capture and conversion[9,34], organic acid products formed from CO_2 reduction[35,36], and ammonium in wastewater remediation[8]). **Figure 3a** demonstrates the ability of the model to predict the OCP of a FB-BPM with a 1 M H_2SO_4 cation-exchange solution and a mixed anion-exchange solution with total ionic strength of 1 M and varying compositions of KOH or KOAc (denoted as a 1 M K(OH + OAc) | 1 M H_2SO_4 FB-BPM), where OAc^- is a weak buffer impurity relevant to electrochemical CO_2 reduction systems.[30] As shown above for the pure electrolytes, these mixed electrolyte OCPs also result from dynamic balancing of co-ion crossover and nonequilibrium acid-base recombination.

Because there are now two competitive anions that can recombine and dictate the OCP, ion-selective partitioning was considered (see **Methods**) using a fitted binary selectivity parameter ($S_{\mathrm{OH}}^{\mathrm{OAc}}$, **Supplementary Note 5**) that controls the selectivity of the AEL to either OH^- or OAc^-. Values of $S_{\mathrm{OH}}^{\mathrm{OAc}} > 1$ denote the AEL is selective to OH^-, values of $S_{\mathrm{OH}}^{\mathrm{OAc}} < 1$ denote the AEL is selective to OAc^-, and values of $S_{\mathrm{OH}}^{\mathrm{OAc}} = 1$ denote equal partitioning (*i.e.,* Donnan equilibrium) (**Supplementary Figure 9**). The fitted value of $S_{\mathrm{OH}}^{\mathrm{OAc}} = 0.18$ denotes that the AEL is far more selective to OAc^- than OH^-, consistent with prior experimental study of ion-selectivity in AELs[37] (**Figure 3b**). Past work has demonstrated that ion-selective partitioning is driven by differences in the strength of physical interactions between the membrane and absorbed counter-ion (**Figure 3c**).[38] While prior work theorized that the curvature and inflection point of the experimentally measured 1 M K(OH + OAc) | 1 M H_2SO_4 FB-BPM OCP curve could be explained by differences between OH^- and OAc^- diffusion coefficients,[17] considering the difference in diffusion coefficients alone is insufficient to predict the experimentally measured behavior (**Figure 3a,** light grey line). Nonideal ion/membrane interactions are thus required to explain measured OCP data and to reproduce the inflection point at the measured % OAc^- in the electrolyte (**Figure 3a,** black line).

Fundamentally, these simulations demonstrate that as the fraction of weak buffer within the electrolyte increases, the OCP decreases from its maximum value corresponding to the recombination of H^+ and OH^- because OAc^- competes with OH^- for sites in the junction and reduces the OCP through neutralization short-circuiting. Accordingly, to maximize OCP, strategies must be employed to eliminate the AEL's preference for the weak buffer. As shown in **Figure 3a**, a FB-BPM with an $S_{\mathrm{OH}}^{\mathrm{OAc}} = 1$ can maintain a larger OCP across a much broader range of anion-exchange solutions. Hence, improving selectivity to H^+ and OH^- over buffering impurities could mitigate the effects of neutralization short-circuiting with mixed electrolytes.
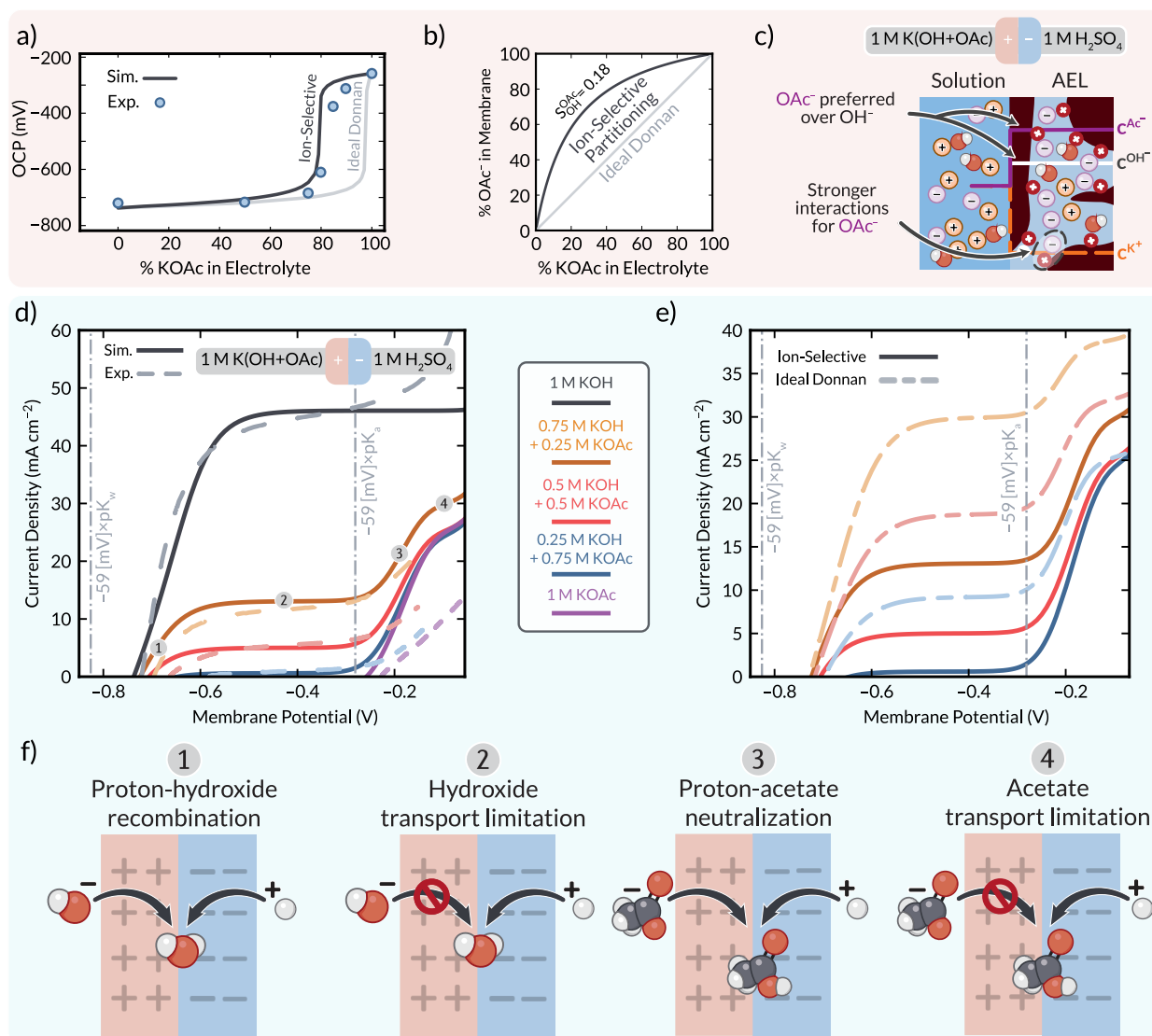
Figure 3: *Theory identifies losses in energy recovery for FB-BPMs with competitive counter-ions.* **(a)** Experimentally measured (markers) and theoretically calculated (solid lines) open-circuit potential (OCP) as a function of the percentage of KOAc in the electrolyte for a 1 M K(OH + OAc) | 1 M H₂SO₄ BPM, assuming both ion-selective partitioning (black) and ideal Donnan behavior (light grey) in the anion-exchange layer (AEL). **(b)** Ion partitioning curve for an AEL that behaves by ideal Donnan (light grey) and with ion-selective partitioning (black). **(c)** Schematic picture of the physical picture through which the AEL preferentially uptakes OAc⁻ over OH⁻. **(d)** Experimentally measured (dashed lines) and theoretically calculated (solid lines) polarization curves for a 1 M K(OH + OAc) | 1 M H₂SO₄ BPM. **(e)** Simulated polarization curves for a 1 M K(OH + OAc) | 1 M H₂SO₄ BPM assuming ion-selective partitioning (dark, solid lines) and ideal Donnan (light, dashed lines) in the AEL. **(f)** Schematic picture illustrating transport mechanisms in FB-BPMs. The number labels for each mechanism in **(f)** correspond to regions of the polarization curve marked in **(d)**. For all experimental data considered, a reference potential drift of 0.045 V was assumed (**Supplementary Note 14**).

9

FB-BPMs must achieve a high OCP and limiting current density to enable power densities relevant for energy recovery and electrocatalysis in an industrial setting. **Figure 3d** demonstrates the power of the model to predict properly the limiting current densities of 1 M K(OH + OAc) | 1 M H_2SO_4 FB-BPMs with varying anion-exchange solution compositions. Importantly, the model demonstrates that these limiting current densities are purely controlled by transport of the recombining ions—neither the presence of the buffer kinetics nor the catalytic enhancement has a meaningful impact of the observed limiting current density (**Supplementary Notes 10** and **11**). Modeling reveals that limiting current densities are strongly controlled by ion-selective partitioning and fixed-charge neutralization of the AEL, wherein OH^- from the anion-exchange solution neutralizes AEL fixed-charge (**Supplementary Figure 11**), reducing the effective number of sites available for recombination (**Supplementary Note 12**). Neutralization of fixed-charge is dictated by the pK_b of the AEL, fit here to a value of 0.5, again consistent with prior reported pK_bs of AELs[39], which suggests that the positively-charged moieties in the AEL are strongly basic, but can be neutralized when the concentration of OH^- is sufficiently high.[40]

Our analysis shows that ion-selective partitioning and fixed-charge neutralization define the available fixed-charge in the FB-BPM, which, in turn, dictates achievable recombination rates (**Figure 3e**; **Supplementary Note 13**). Collectively, these results reveal a more complex picture than simple ideal-Donnan site competition,[29] underscoring the importance of nonideal interactions between absorbed ions and the membrane that inhibit H^+/OH^- recombination. Hence, highly basic AELs or acidic CELs that are selective to OH^- or H^+, respectively, are required to ameliorate these effects and enable high rates of recombination.

Beyond understanding the processes that dictate limiting current densities in FB-BPMs, the model also elucidates the underlying physical processes in the polarization curve through analysis of the modeled concentration profiles and fractional current densities (**Figure 3f, Supplementary Figures 11–15**). At low current densities, within the kinetically controlled regime of FB-BPM performance, the recombination of H^+ and OH^- dominates (1). The limiting current density for this reaction is achieved when OH^- is depleted at the AEL|CL interface (2), forming a voltage-independent current plateau that is flat until the onset of H^+ and OAc^- recombination (3). Finally, this reaction becomes transport limited once OAc^- at the junction is depleted (4).

In real systems with strong base, a concern is the absorption of atmospheric CO_2 into the AEL as CO_3^{2-}.[41,42] CO_3^{2-} is a particularly deleterious competitive buffering anion, due to its divalent nature that highly encourages its absorption in the AEL over OH^-.[38] Hence, even miniscule concentrations of CO_3^{2-} in the anion-exchange solution can significantly reduce the available fixed AEL sites for OH^- transport (**Supplementary Figure 16**), and, in turn, the current and power density of FB-BPMs. As shown in **Figure 4a–b**, the simulation predicts that even in an ideal 1 M KOH | 1 M HCl FB-BPM with no fixed-charge neutralization or ion-selective partitioning, absorption of 1 mM CO_3^{2-} in the anion-exchange solution reduces achievable current and power densities by 50%.

This is exacerbated for a 1 M KOH | 1 M H_2SO_4 FB-BPM, where the HSO_4^- anion can crossover and contribute to parasitically buffering the interface (**Figure 4c–d**), which occurs because the HSO_4^- anion will preferentially dissociate at any potential more negative than 0.059 [V] $\times pK_{a,HSO_4^-} = -0.12$ [V]. This HSO_4^- dissociation contributes negative current density, which

attenuates the recombination rate. More importantly, the generated SO_4^{2-} significantly reduces H^+/OH^- recombination due to its divalent nature occupying twice as much fixed charge in the AEL. This demonstrates the importance of operating with co-ions that cannot dissociate (*e.g.*, Cl^-).

Importantly, the more alkaline the anion-exchange solution, the more it captures CO_2, thereby exacerbating the above effect, similar to fixed-charge neutralization. Due to the extreme sensitivity of FB-BPM performance to CO_2 uptake, and the similarities in its behavior to fixed-charge neutralization, further experimental studies of FB-BPM limiting currents in CO_2-free environments will be required to deconvolute the effects of CO_2 uptake and fixed-charge neutralization. As it stands, the fitted pK_b value, while consistent with literature ranges, could be compensating for CO_2 absorption. Nonetheless, the above analysis resolves key phenomena that underpin the FB-BPM polarization curve and provides new understanding of the substantial roles various nonideal physical phenomena (ion-selective partitioning, fixed-charge neutralization, and CO_2 uptake) play in dictating achievable currents in FB-BPMs.
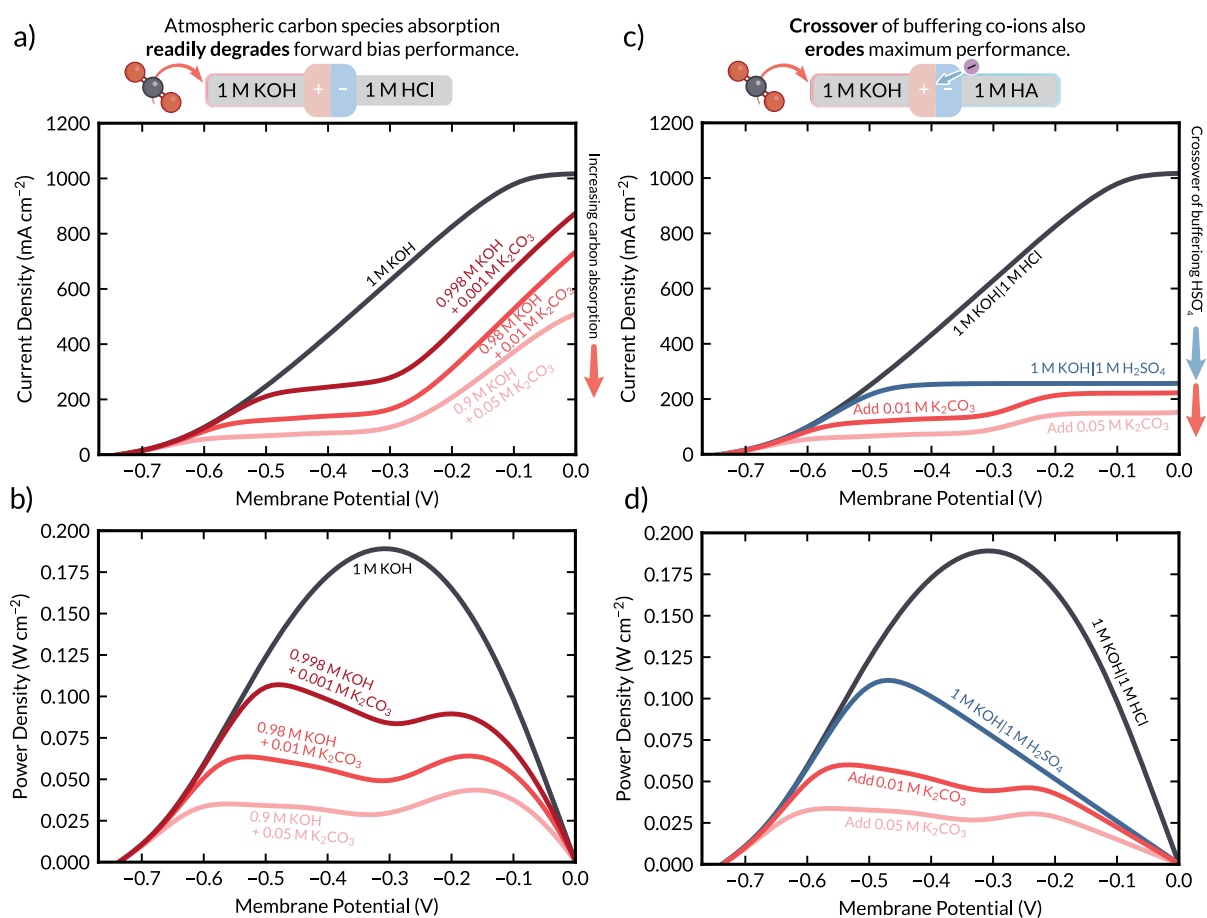

Figure 4: *CO_2 absorption and co-ion crossover severely attenuates current and power density in FB-BPMs.* Impact of carbonate anion impurities on the simulated **(a)** limiting current density and **(b)** power density of a 1 M KOH | 1 M HCl FB-BPM. Impact of co-ion crossover and dissociation on the simulated **(c)** limiting current density and **(d)** power density of 1 M KOH | 1 M H$_2$SO$_4$ FB-BPM. In these simulations, the FB-BPM is considered unselective with no fixed-charge neutralization.

2.3 Operation of forward-bias BPMs in over-limiting regimes

CO_2 electrolyzers are capable of operating at current densities beyond 100 mA cm^{-2} with FB-BPMs despite the transport-limited current density of ~10 mA cm^{-2} for FB-BPM HCO_3^-/H^+ recombination.[17,43,44] To understand this so-called "over-limiting behavior", a simple 1 M KOH | 1 M HCl FB-BPM without fixed-charge neutralization was simulated over a wider range of voltages (–0.8 V < V_{BPM} < +0.4 V, **Figure 5a-e**). As can be seen in **Figure 5e**, at applied voltages where net voltage is applied (V_{BPM} > 0 V), the FB-BPM current density can exceed that dictated by its mass-transfer-limited plateau in the regime where voltage is recovered (V_{BPM} < 0 V).

This over-limiting behavior occurs because when excess voltage is applied, the external potential gradient (*i.e.*, the macroscopic electric field) changes direction (**Figure 5c**), enhancing the transport of counter-ions by electromigration and enabling improved recombination rates (**Figure 5d-e**). This improved transport of OH^- to the CL by migration is evidenced by the fact that the OH^- concentration in the AEL is higher at V_{BPM} = +0.3 V than it is at V_{BPM} = 0.0 V, despite the consumption of OH^- anions by recombination being greater at V_{BPM} = +0.3 V (**Figure 5b**). Additionally, the current-voltage characteristics in the over-limiting regime are controlled solely by the transport properties of the FB-BPM (**Supplementary Note 15**). These results reveal that FB-BPMs operating beyond their current density plateau require additional voltage input to drive ion transport. This additional voltage is analogous to the ohmic resistance in monopolar membrane, where a potential gradient is used to drive ion transport. Nonetheless, less voltage is required to drive a given current density with a FB-BPM than a monopolar AEM due to voltage recovery from the sustained local environments (**Supplementary Figure 59**).

Extending this analysis to multi-ion FB-BPMs shows that this over-limiting behavior applies also to the recombination of buffering anions with H^+ to form neutral species (**Figure 5f-g**). For instance, in a 1 M KHCO$_3$ | 1 M H$_2$SO$_4$ FB-BPM, HCO_3^- and H^+ recombine within the CL to form neutral CO_2. As stated above, this recombination reaction is mass-transport limited to ~10 mA cm^{-2}, which means that the beyond this current density the concentration of reactants in the recombination reactions go to zero. However, current densities beyond the mass-transport limit can be achieved by applying positive membrane potential to increase the transport of the recombination reactants to the interface by migration, explaining how FB-BPM CO_2 electrolyzers can operate at current densities exceeding 100 mA cm^{-2} despite being (bi)carbonate exchanged.

Unfortunately, in this case, we find that neutral CO_2 formed at the AEL|CEL interface by recombination can diffuse out of either membrane, leading to a net crossover of carbon from the AEL-exchange solution to the CEL-exchange solution in the over-limiting regime (**Supplementary Note 16**).[17] Additionally, the generated CO_2 gas from HCO_3^-/H^+ recombination can pressurize the interface and lead to delamination of the FB-BPM,[44] motivating the need for better control of recombination to improve stability. Similarly, if a CO_2 electrolyzer is generating a value-added liquid product (*e.g.*, formate ($HCOO^-$) or acetate (OAc^-)), that product can be lost by recombination with H^+ in the CL and subsequent crossover of the generated neutral species through the CEL (**Supplementary Note 17**). Accordingly, these analyses demonstrate that over-limiting transport of counter-ions also accelerates the cross-over of carbon species or liquid-phase electrosynthesis products through the FB-BPM.
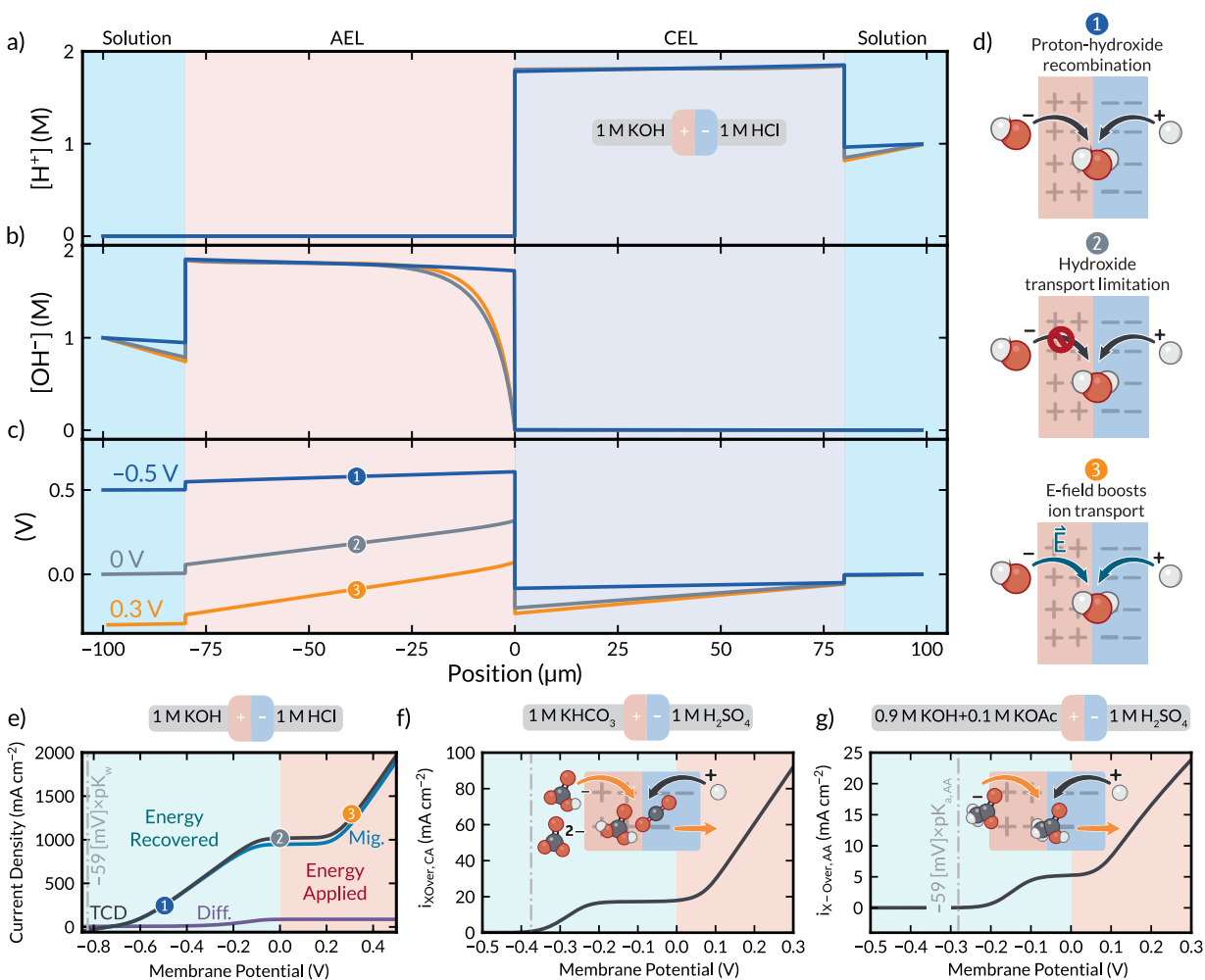
Figure 5: *Modeling reveals the nature of limiting and over-limiting current density in forward-biased bipolar membranes (FB-BPMs).* Concentration profiles of **(a)** H^+ and **(b)** OH^-, and **(c)** electrostatic potential profiles of a 1 M KOH | 1 M HCl BPM operating up to 2 A cm^{-2}. **(d)** Schematic representation of transport mechanisms in FB-BPMs. **(e)** Polarization curve of a 1 M KOH | 1 M HCl FB-BPM operating up to 2 A cm^{-2}, with current density broken down into contributions associated with migration-driven transport (blue) and diffusion-driven transport (purple). **(f)** Over-limiting CO_2 crossover in a 1 M KHCO$_3$ | 1 M H$_2$SO$_4$ FB-BPM. **(g)** Over-limiting acetic acid crossover in a 0.9 M KOH + 0.1 M KOAc | 1 M H$_2$SO$_4$ FB-BPM. In **(e–g)**, the teal region corresponds to current densities for where voltage is recovered, the red region corresponds to a regime where there is net voltage input across the FB-BPM. The number labels for each mechanism in **(d)** correspond to regions of the polarization curve marked in **(e)**.

2.4 Sensitivity of forward-bias performance to electrolyte and bipolar membrane properties

Finally, we performed sensitivity analyses of the FB-BPM performance to various properties of the membranes and electrolyte to reveal the greatest opportunities for tailoring materials and electrolytes for FB-BPM operation. First, an applied-voltage-breakdown analysis[45]

(**Supplementary Methods**) of a simplified 1 M KOH | 1 M HCl FB-BPM (**Figure 6a**) is conducted to identify the dominant performance losses of a FB-BPM in the absence of nonideal multi-component phenomena (*e.g.*, neutralization short-circuiting, ion-selective partitioning, and fixed-charge neutralization)—in other words, assuming perfect management of ionic impurities. This analysis revealed that recombination kinetic losses are dominant at low current densities for H^+ and OH^- recombination. However, at higher current densities, potential losses through the AEL and CEL (primarily due to ohmic resistance) become dominant.

A sensitivity analysis of the maximum achievable power density to the thicknesses of the individual ion-exchange layers was carried out by simulating 1 M KOH | 1 M HCl FB-BPMs for various AEL or CEL thicknesses. **Figure 6b** reveals local optima in AEL thickness for a given CEL thickness (or *vice versa*). This nontrivial optimization landscape with respect to thickness occurs because, at a given thickness of the CEL, a thinner AEL helps improve transport of OH^- to the junction for recombination. However, if the AEL becomes too thin, H^+ can leak through the thin AEL prior to recombination due to insufficient Donnan exclusion. This analysis reveals tradeoffs between transport and crossover when modulating ion-exchange layer thicknesses in FB-BPMs. Sensitivity analysis to the fixed-charge of the individual ion-exchange layers in a 1 M KOH | 1 M HCl FB-BPM is much simpler (**Figure 6c**). Higher fixed-charge of a given ion-exchange layer always results in improved power-density for a FB-BPM since increasing the fixed-charge increases the number of sites available to mediate transport of recombining counter-ions while also improving Donnan exclusion and mitigating parasitic co-ion leakage.

Critically, this analysis demonstrates that acid/base recombination power densities approaching 1 W cm^{-2} are achievable through rational material design. Thus, the optimal management of ionic impurities could enable power densities over an order of magnitude larger than previously reported for the recombination of 1 M acid and base in a FB-BPM.[17,46,47] These results motivate the development and implementation of high-fixed charge polymers for FB-BPMs.[48] However, research is required to maintain mechanical stability of these high-fixed charge density polymers, as the mechanical integrity of ion-conducting polymers is compromised at extremely high fixed-charge densities.[49]

Applied-voltage analysis was also performed on a more complex multi-component 0.5 M KOH + 0.5 M KOAc | 1 M H$_2$SO$_4$ FB-BPM, to understand the role of materials engineering in scenarios where multi-ion behavior is not negligible (**Figure 6d**). In this system, it is observed that nonideal phenomena associated with multi-ion competition for sites in the polymer and fixed-charge neutralization induce substantial mass-transport resistances for H^+/OH^- recombination. Due to the computational intensity of the multi-component simulation, rather than simulating numerous discrete BPMs for every sensitivity variable, a gradient-based sensitivity analysis was performed over the key variables that dictate performance (see **Supplementary Methods**).

In this analysis, the value of sensitivity of an output j to and input i, κ_{ij}, is defined as the factor by which j changes for a given increase in i, with the sign of κ_{ij} denoting if the output increases or decreases. For instance, if κ_{ij} is +2, then j increases by a factor of 4 when i increases by a factor of 2. If κ_{ij} is –2, then j decreases by a factor of 4 when i increases by a factor of 2. For FB-BPM performance to be maximized, we aim to increase the limiting current density while minimizing parasitic co-ion crossover.
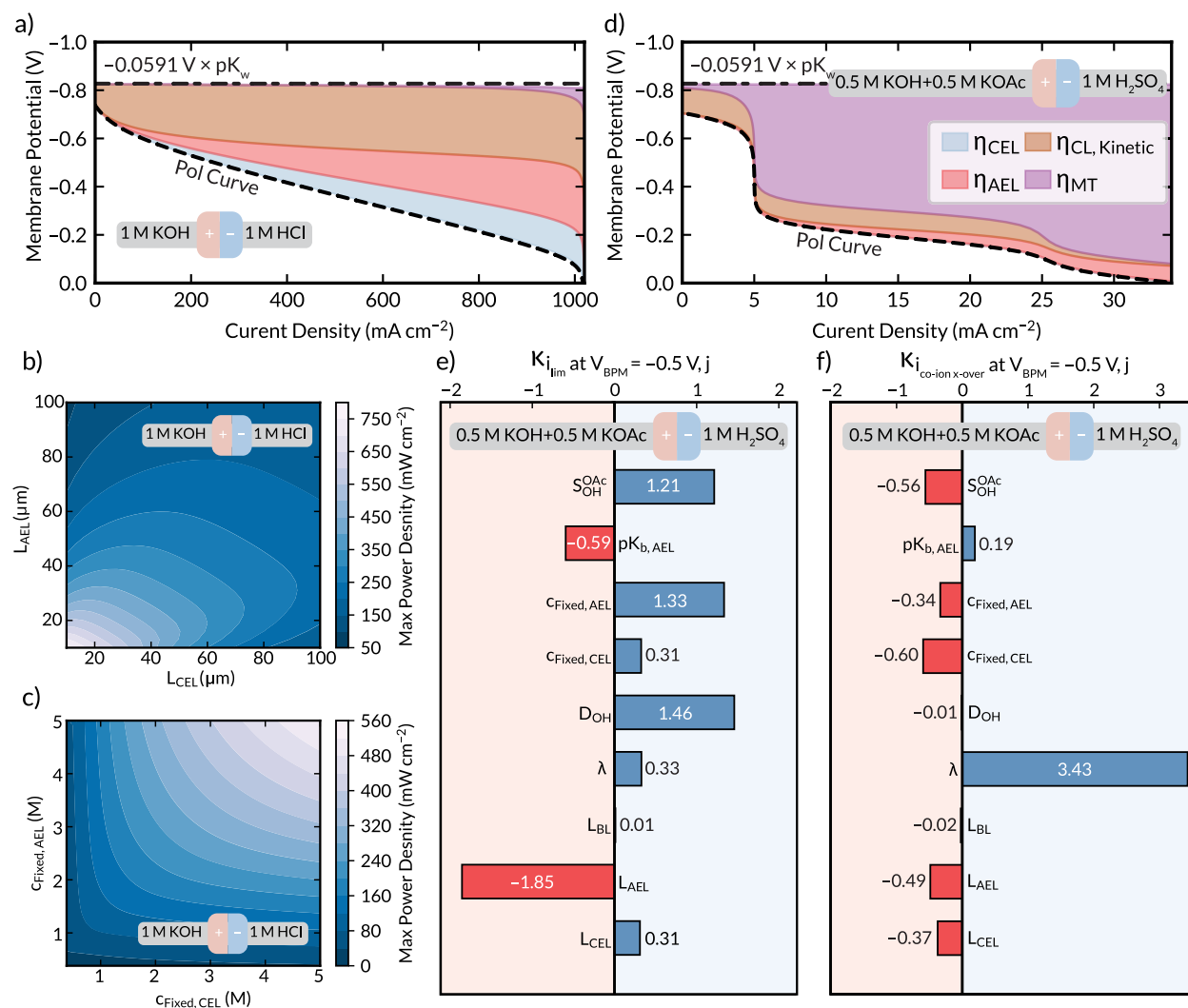
14

Figure 6: *Voltage loss and sensitivity analysis reveal dominant losses and opportunities for future engineered materials.* Applied-voltage-breakdown analysis (**Supplementary Methods 4**) for an **(a)** idealized 1 M KOH | 1 M HCl FB-BPM, and a **(b)** mixed composition 0.5 M KOH + 0.5 M KOAc | 1 M H_2SO_4 FB-BPM. Contour plots demonstrating the simulated maximum power density for the idealized 1 M KOH | 1 M HCl FB-BPM of varying **(c)** AEL or CEL thickness and **(d)** AEL or CEL fixed-charge. Sensitivity analysis (**Supplementary Methods 3**) of the **(e)** limiting current density and **(f)** co-ion crossover in a mixed composition 0.5 M KOH + 0.5 M KOAc | 1 M H_2SO_4 FB-BPM to various membrane and electrolyte properties. The effect of the parameters in **(e)** and **(f)** to the full polarization curves are shown in **Supplementary Figures 17-24**.

Our sensitivity analyses of limiting current density and co-ion crossover (**Figure 6e-f**) to membrane and electrolyte properties reveal that significant performance improvements can be achieved by increasing fixed-charge of either ion-exchange layer, reducing the AEL pK_b to mitigate fixed-charge neutralization, and increasing the selectivity of the AEL to OH^- over OAc^-. Other strategies, such as reducing the AEL thickness or increasing the water uptake of the FB-BPM, improve limiting current densities at the cost of increased co-ion leakage. This analysis

highlights that selective, highly charged polymers, with robust fixed-charge are key to enabling next-generation systems that employ FB-BPMs. This analysis also underscores how chemical engineering approaches can guide material design and integration.

2.5   Implications for the Design of FB-BPM Systems for Energy Recovery

The analysis presented in this work highlights the substantial, deleterious impacts of multi-component phenomena on energy recovery in FB-BPMs. The pernicious impacts of CO_2 absorption on H^+/OH^- recombination delineated in **Figure 4** reveal that any FB-BPM fuel cell or acid-base recombination cell must be operated in a CO_2-free environment to achieve meaningful current and power densities. Additionally, the substantial effects of ion-selective partitioning and fixed-charge neutralization determined by the established theory reveal significant potential challenges with ion-management for systems that aim to extract voltage both from redox chemistry and acid-base recombination (*e.g.,* acid-base redox-flow batteries[23,25]). Such systems could achieve industrially-relevant power densities by leveraging size-selective ion-conducting polymers that are selective to H^+/OH^- while simultaneously rejecting sterically larger redox-active molecules.[50] However, more work is needed on the development of such materials. Collectively, this work demonstrates that managing multi-ion transport to enhance the selectivity and kinetics of H^+/OH^- recombination should be of paramount focus in future research.

2.6   Implications for the Design of FB-BPM Systems for CO_2 Electrolysis

For CO_2 electrolysis systems that employ FB-BPMs, the analysis reveals that not only do multi-ion effects limit the current density that can be achieved while still extracting voltage from acid-base recombination, but also that the recombination of (bi)carbonates with protons to form neutral CO_2 enables an alternative mechanism of CO_2 generation and crossover in FB-BPMs. Similarly, parasitic recombination reactions can also lead to the net-crossover of liquid-phase products generated at the cathode in a FB-BPM CO_2 electrolyzer. Accordingly, our analysis suggests that while FB-BPMs do reduce CO_2 and neutral product crossover compared to monopolar AEMs, they are worse at mitigating crossover than RB-BPMs (**Supplementary Notes 18-19**). This suggests that RB-BPMs are preferred for CO_2 electrolysis if maximizing single-pass conversion is vital. However, on the basis of the membrane potential required to drive ionic current, the FB-BPM requires less voltage to maintain a given current than both the monopolar AEM and the RB-BPM, suggesting the existence of a trade-off in reactor design between the energy requirement of the ionic separator and its ability to ameliorate crossover.

We note, however, that there are scenarios for which the acidic cathode environment of an RB-BPM limits selectivity to value-added products (*e.g.,* CO over Ag catalysts or C_{2+} products over Cu catalysts),[51] necessitating use of a FB-BPM. In such cases, an asymmetric FB-BPM with a thin AEL improves anion transport while also encouraging back-diffusion of generated neutral species to mitigate crossover (**Supplementary Note 20**). Such membranes have been demonstrated for water management[52], and have recently been shown to similarly direct neutral species out of the FB-BPM, thereby allowing for a pressure outlet at the AEL|CEL interface to ameliorate gas-induced delamination.[44,53]

3. Conclusions

Forward-biased bipolar membranes (FB-BPMs) possess substantial promise for application in energy storage and conversion systems due to their ability to extract electrical voltage from gradients in pH or chemical potential. These materials can reduce energy consumption and facilitate optimal chemical environments for CO_2 electrolysis, enable self-humidification in H_2 fuel cells, and augment achievable voltages in redox-flow batteries. However, despite these immense advantages, the underlying physics that govern the behavior of FB-BPMs in these complex, multi-component systems are still poorly understood.

In this study, we develop an experimentally validated continuum model based on chemical engineering principles of thermodynamics, transport, and kinetics that can predict the performance of FB-BPMs exchanged with a wide assortment of multi-component electrolytes for energy recovery. The model reveals the importance of considering nonideal phenomena when evaluating the performance of FB-BPMs. In particular, we show that OCP in FB-BPMs occurs when the rate of co-ion crossover matches the rate of counter-ion recombination, that ion-selective partitioning driven by physical ion/membrane interactions causes impurities to outcompete OH^- and H^+ for fixed-charge groups, and that OH^- can neutralize fixed-charges in the AEL. All of these phenomena attenuate achievable power density. The simulations also reveal that energy cannot be extracted from FB-BPMs operating at current densities beyond the mass-transport limited current plateau (*i.e*, the maximum recombination rate in the absence of a potential gradient), and that instead excess voltage must be applied to encourage counter-ion transport by migration. Sensitivity analysis establishes that the greatest area of opportunity for future development of FB-BPM systems is H^+/OH^- selective BPMs with high concentrations of robust fixed charge ($pK_{b,AEL}$, $pK_{a,CEL} < 0$), suggesting that such materials could achieve power densities over an order of magnitude larger than those previously reported for acid/base recombination.

Lastly, the implications of the results are discussed for various applications. For energy storage, where CO_2-free operation is required and size-selective polymers that block transport of bulky redox active species could mitigate competition for charged-sites. In CO_2 electrolysis, asymmetric FB-BPMs with thin AELs can mitigate crossover of liquid-phase products or CO_2 by promoting transport of generated neutral species to the AEL-exchange solution from which they originate. Altogether, the established theory unveils the role of multi-component phenomena in FB-BPMs and elucidates a new ceiling for performance that can be unlocked by rational materials design and ion management, opening the door for FB-BPMs to achieve their immense potential as next-generation energy materials and assemblies.
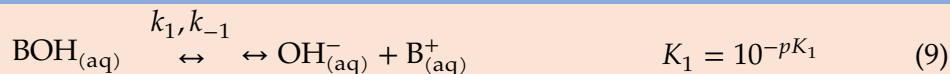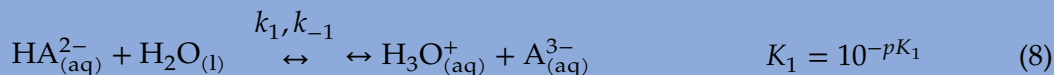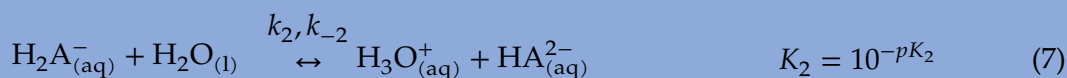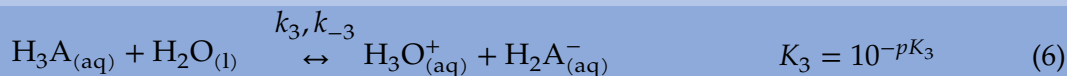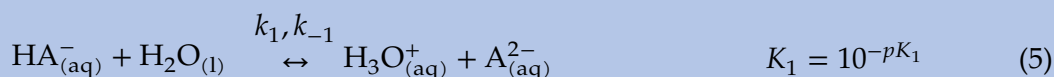
4. Methods

4.1 Model Framework

The continuum model was developed based on the reverse-bias BPM model reported previously by Bui *et al.* for buffered multi-component electrolytes.[27] This framework simulates 4-probe experiments performed for direct BPM analysis (**Supplementary Figure 5**),[26] using a 1-dimensional (1-D) continuum representation of a BPM containing an 80 µm CEL, a 2.7 nm CL, and an 80 µm AEL, with 20 µm exchange-solution (ES) boundary layers (BLs) on each side of the

BPM (**Figure 1a**). Modeling the domain as such resolves all concentration profiles and species fluxes within the BPM and adjacent diffusion BLs. The effects of forced convection are considered implicitly through the BL thickness. However, convective effects are not modeled, because the model is 1-D in the direction perpendicular to the direction of flow. It is important to note that experiments were conducted at ambient temperature (298 K).[54] Hence, all simulations in this study were isothermal at this same temperature. Detailed description of the experimental methods can be found in the articles where the experimental data were first presented.[17,18]

Crucial to reproducing experimentally observed behavior is the explicit consideration of non-equilibrium generation and consumption of species *via* the homogeneous buffer reactions shown below.

$$2\mathrm{H_2O_{(l)}} \overset{k_w, k_{-w}}{\leftrightarrow} \mathrm{H_3O^+_{(aq)}} + \mathrm{OH^-_{(aq)}} \qquad K_1 = 1 \times 10^{-14} \qquad (2)$$

$$\mathrm{HA_{(aq)}} + \mathrm{H_2O_{(l)}} \overset{k_1, k_{-1}}{\leftrightarrow} \mathrm{H_3O^+_{(aq)}} + \mathrm{A^-_{(aq)}} \qquad K_1 = 10^{-pK_1} \qquad (3)$$

$$\mathrm{H_2A_{(aq)}} + \mathrm{H_2O_{(l)}} \overset{k_2, k_{-2}}{\leftrightarrow} \mathrm{H_3O^+_{(aq)}} + \mathrm{HA^-_{(aq)}} \qquad K_2 = 10^{-pK_2} \qquad (4)$$

$$\mathrm{HA^-_{(aq)}} + \mathrm{H_2O_{(l)}} \overset{k_1, k_{-1}}{\leftrightarrow} \mathrm{H_3O^+_{(aq)}} + \mathrm{A^{2-}_{(aq)}} \qquad K_1 = 10^{-pK_1} \qquad (5)$$

$$\mathrm{H_3A_{(aq)}} + \mathrm{H_2O_{(l)}} \overset{k_3, k_{-3}}{\leftrightarrow} \mathrm{H_3O^+_{(aq)}} + \mathrm{H_2A^-_{(aq)}} \qquad K_3 = 10^{-pK_3} \qquad (6)$$

$$\mathrm{H_2A^-_{(aq)}} + \mathrm{H_2O_{(l)}} \overset{k_2, k_{-2}}{\leftrightarrow} \mathrm{H_3O^+_{(aq)}} + \mathrm{HA^{2-}_{(aq)}} \qquad K_2 = 10^{-pK_2} \qquad (7)$$

$$\mathrm{HA^{2-}_{(aq)}} + \mathrm{H_2O_{(l)}} \overset{k_1, k_{-1}}{\leftrightarrow} \leftrightarrow \mathrm{H_3O^+_{(aq)}} + \mathrm{A^{3-}_{(aq)}} \qquad K_1 = 10^{-pK_1} \qquad (8)$$

$$\mathrm{BOH_{(aq)}} \overset{k_1, k_{-1}}{\leftrightarrow} \leftrightarrow \mathrm{OH^-_{(aq)}} + \mathrm{B^+_{(aq)}} \qquad K_1 = 10^{-pK_1} \qquad (9)$$
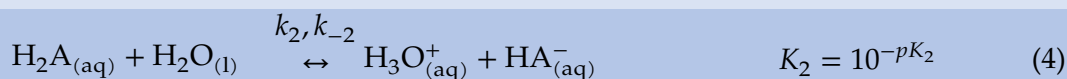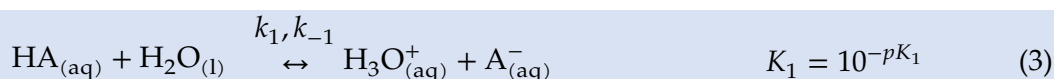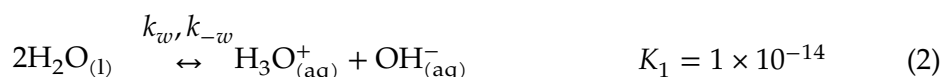
Due to the large variety of electrolytes considered in this study, the acid dissociation/recombination reactions shown above have been written for generic monoprotic **(eq. (3))**, diprotic **(eq. (4)–(5))**, or triprotic acids **(eq. (5)–(7))**, as well as monovalent bases **(eq. (9))**. The equilibrium constants for each dissociating species were taken from literature pK$_{a/b}$'s and converted to equilibrium constants by the relation $K_i = 10^{-pK_i}$, where pK_i is the pK$_a$ or pK$_b$ of a given proton or hydroxide transfer event, respectively. All equilibrium constants and pK$_{a/b}$'s are shown in **Supplementary Table 3.**

4.2 Thermodynamics of Forward-Bias Bipolar Membranes

The following expression for electrochemical potential (μ_i) is used to describe the thermodynamics of all relevant species,[28,55]

$$\mu_i = \mu_i^0 + RT\ln(a_i) + z_i F\Phi, \tag{10}$$

where Φ is the electrostatic potential. R is the ideal gas constant. T is the absolute temperature, and F is Faraday's constant. In Equation (10), the first term defines the reference chemical potential (μ_i^0), the second term accounts for changes in the activity of a given species, and the third term accounts for electrostatic potential and only has a non-zero value for charged species (*i.e.*, all species except neutral acids/bases).

Activity (a_i) is defined by

$$a_i = \frac{\gamma_i c_i c_{\mathrm{H_2O}}^0}{c_{\mathrm{ref}} c_{\mathrm{H_2O}}}, \tag{11}$$

where c_i is the concentration of a given species i, $c_{\mathrm{H_2O}}$ is the concentration of water, and $c_{\mathrm{H_2O}}^0 = 55.56\,M$ is the molar concentration of pure water. All concentrations are given based on a superficial basis (*i.e.*, normalized by total volume of membrane swollen with water). c_{ref} is a reference concentration (1 M), and the ratio $c_{\mathrm{H_2O}}/c_{\mathrm{H_2O}}^0 = \varepsilon_{\mathrm{w}}$ accounts for the volume fraction of water within the BPM. The inclusion of this volume fraction within the activity definition denotes that equilibrium reactions occur within interstitial liquid-filled volumes of the polymer. The activity coefficient, γ_i, can be decomposed into a product of activity coefficients that result from various effects. In this work, the nonideal contributions considered are electric-field effects and ion-selective partitioning,

$$\gamma_i = \gamma_{i,\mathrm{SWE}}(E)\gamma_{i,\mathrm{partition}}, \tag{12}$$

For neutral species and ions that do not participate in acid/dissociation recombination reactions (*i.e.*, K$^+$), the Second Wien Effect (SWE) activity coefficient ($\gamma_{i,\mathrm{SWE}}(E)$) is not a function of electric field (*i.e.*, $\gamma_{i,\mathrm{SWE}}(E) = 1$). For charged species that participate in dissociation/recombination reactions, the electric-field-dependent activity coefficient preserves macroscopic equilibrium (**Supplementary Note 1**),

$$\gamma_{i,\mathrm{SWE}}(E) = \sqrt{f(E)}^{-|z_i|}, \tag{13}$$

where $|z_i|$ is the absolute value of the charge on species i, E is the local electric field, and $f(E)$ is the dependence of the macroscopic equilibrium constant on electric field:[56–60]

$$f(E) = \frac{\exp(\alpha_{\mathrm{WD}}\beta E)}{1 + \frac{1-\exp\left(-\frac{1}{\sigma}\right)}{2}\left(\sigma^2\beta E + (4.97\sigma)\frac{\sinh(0.0835\sigma\beta E)}{\cosh^2(0.0835\sigma\beta E)}\right)}. \tag{14}$$

where β, τ, and σ are lumped parameters, and α_{WD} is a fitted parameter similar to the transfer coefficient in Butler-Volmer kinetics that describes the sensitivity of the WD catalysis to electric field (discussed in **Supplementary Methods**). The exponential dependence of the numerator on

E is a simplified expression that has been shown to approximate well the Bessel-function-type Onsager Second Wien Effect dependence.[4,59] Accordingly, equilibrium constants of dissociation/recombination reactions are defined as
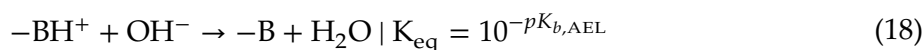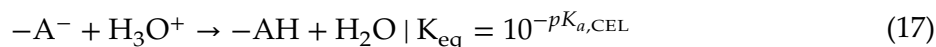
$$K_n(E) = K_n(E = 0)f(E) \tag{15}$$

where $K_n(E)$ is the local equilibrium constant for a homogeneous dissociation reaction that depends on local electric field, and $K_n(E = 0)$ is its value under no field.

Additionally, the fixed charge in the BPM dictates its ability to absorb counter-ions and reject co-ions by Donnan equilibrium (**Supplementary Notes 3–4**). This fixed charge is given by the following hyperbolic tangent expression.

$$c_M(x) = \frac{\rho_{M,wet} \times IEC}{2}\left(\xi_{AEL}\left(\tanh\left(\frac{x - x_1}{L_{char}}\right) - \tanh\left(\frac{x - x_2}{L_{char}}\right)\right)\right.$$
$$\left. - \xi_{CEL}\left(\tanh\left(\frac{x - x_3}{L_{char}}\right) + \tanh\left(\frac{x - x_4}{L_{char}}\right)\right)\right) \tag{16}$$

where $\rho_{M,wet}$ and IEC are the wet membrane density and ion-exchange capacity, respectively, provided in **Supplementary Table 5**, x_1 is the leftmost position of the AEL, x_2 is the right most position of AEL, x_3 is the leftmost position of CEL, and x_4 is the rightmost position of the CEL. Per this definition, the AEL possesses positive fixed charge, and the CEL possesses negative fixed charge of equal concentration to the positive fixed charge in the AEL. The hyperbolic tangent ensures smooth transitions between regions to encourage convergence.[27] $(1 - \xi_{AEL})$ and $(1 - \xi_{CEL})$ are the fraction of the AEL or CEL fixed charge that has been neutralized by OH⁻ or H⁺, respectively.[40] Hence, ξ_{AEL} and ξ_{CEL} represent the fraction of available fixed charge in the BPM.

The neutralization of this fixed charge can occur in the domain for BPMs exchanged with highly concentrated acid or base as shown by Andersen *et al.*[40]

$$-A^- + H_3O^+ \rightarrow -AH + H_2O \,|\, K_{eq} = 10^{-pK_{a,CEL}} \tag{17}$$

$$-BH^+ + OH^- \rightarrow -B + H_2O \,|\, K_{eq} = 10^{-pK_{b,AEL}} \tag{18}$$

where $-A^-$ is a fixed negative charge group in the CEL and $-BH^+$ is a fixed positive charge group in the AEL. $pK_{a,CEL}$ is the pKₐ of the fixed charge groups in the CEL, and $pK_{b,AEL}$ is the pKᵦ of the fixed charge in the AEL. Using a classical Langmuir adsorption isotherm provides the following expression for ξ_{AEL} and ξ_{CEL}:

$$\xi_{AEL} = \left(1 + \frac{c_{OH^-}}{10^{-pK_{b,AEL}}}\right)^{-1} \tag{19}$$

$$\xi_{CEL} = \left(1 + \frac{c_{H^+}}{10^{-pK_{a,CEL}}}\right)^{-1} \tag{20}$$

According to the above expressions, as the fixed-charge in the AEL and CEL becomes larger (*i.e.*, the AEL has a highly negative pKᵦ or the CEL has a highly negative pKₐ), the effects of fixed-charge neutralization become negligible.

Finally, to model partitioning and ion-selectivity in AELs exchanged with mixed KOAc + KOH electrolytes, an activity coefficient based on the binary selectivity of the polymer is defined for the selectively sorbed OAc⁻ anion within the AEL.

$$\gamma_{i=\text{OAc}^-,\text{partition}} = \begin{cases} S_{\text{OH}}^{\text{OAc}} \text{ within AEL} \\ 1 \text{ outside of AEL} \end{cases}$$

$$\gamma_{i \neq \text{OAc}^-,\text{partition}} = 1$$

(21)

This definition implies that favorable thermodynamic interactions between OAc⁻ and the AEL facilitate the AEL's preference for OAc⁻ over OH⁻ (**Supplementary Note 5**). While these interactions are not directly resolved here, work by Crothers *et al.* suggests that nonideal partitioning is primarily dictated by physical interactions between the absorbed counter-ion and the fixed-charge groups in the polymer.[38] Future work should seek to resolve these effects from first principles.

Fixed-charge neutralization and binary-selectivity effects (Equations (17)–(21)) were only considered for the KOH + KOAc simulations (**Figure 3**), due to the importance of properly calculating the competition for AEL fixed-charge sites to reproduce experimentally observed limiting current densities as a function of electrolyte composition. These effects do not have a significant impact on the OCP simulated for pure electrolyte salts due to low H⁺ and OH⁻ concentrations. Additionally, incorporating binary selectivity would require a fitted binary selectivity for every anion, and this fitting process requires substantial quantities of limiting current density data for each electrolyte tested as described in the **Model Fitting and Validation** section below, and obtaining binary selectivity data is nontrivial for multivalent anion electrolytes such as phosphates or carbonates. Hence, for the pure electrolyte simulations and mixed electrolyte simulations containing electrolytes other than monovalent OAc⁻, simulations were solved using ideal Donnan equilibrium and assuming that ξ_{AEL} and ξ_{CEL} are both unity. We note that these simulations thus overpredict the forward-bias limiting current density by ignoring the effects of fixed-charge neutralization. Nonetheless, these simulations are sufficient to reveal trends in and mechanisms of limiting current density and neutral species crossover for varying electrolyte and membrane compositions. Future work that calculates these binary selectivity coefficients from first principles and the physical properties of dissolved species and polymer will be necessary to capture these effects fully for complex electrolytes beyond KOH + KOAc.

4.3 Kinetics of Forward-Bias Bipolar Membranes

Homogeneous dissociation/recombination reactions generate and consume species throughout the model domain. The volumetric source term for species i due to such reactions is given by the law of mass action:

$$R_{\text{B},i} = k_0 \sum_n s_{i,n} \left(k_n \prod_{s_{i,n}<0} \left(\frac{c_i}{c_{i,\text{ref}}} \right)^{-s_{i,n}} - k_{-n} \prod_{s_{i,n}>0} \left(\frac{c_i}{c_{i,\text{ref}}} \right)^{s_{i,n}} \right)$$

(22)

where $s_{i,n}$ is the stoichiometric coefficient of reactant i in reaction n, k_n is the forward (dissociation) rate constant for the reaction, and k_{-n} is the reverse (recombination) rate constant for the reaction. $c_{i,ref}$ is the reference concentration of species i, which is 1 M for all dissolved

21

species and 55.556 M for water. To model the effect of the catalyst, we treat the CL as a thin neutral region located between the AEL and CEL where a large electric field can drive dissociation chemistry *via* the Second Wien Effect (**eq. (13), (24), and (25)**). Recombination chemistry is primarily driven by mass action.[58,61,62] Within the CL domain, a dimensionless catalytic enhancement factor of $k_0 = 5$ multiples the rate of $R_{B,i}$, and is necessary to replicate the curvature in the FB polarization signature observed by Dinh *et al.*[17] (**Supplementary Figure 2**). Outside of the CL domain, $k_0 = 1$.

Forward and reverse rate constants are related to the macroscopic equilibrium constant by

$$K_i = \frac{k_i}{k_{-i}} \tag{23}$$

The forward and reverse rate constants for dissociation/recombination reactions are impacted by the electric field,

$$\frac{k_n(E)}{k_n(E = 0)} = \exp(\alpha_{WD} \beta E) \tag{24}$$

$$\frac{k_{-n}(E)}{k_{-n}(E = 0)} = 1 + \frac{1 - \exp\left(-\frac{1}{\sigma}\right)}{2}\left(\sigma^2 \beta E + (4.97\sigma)\frac{\sinh(0.0835\sigma\beta E)}{\cosh^2(0.0835\sigma\beta E)}\right) \tag{25}$$

where E is local electric field, σ is dimensionless bond length, βE is the nondimensional electric field, and α_{WD} is a fitting parameter that dictates the sensitivity of the WD kinetics to the field (see **Supplementary Methods** for more detail). For reactions where the rate constants have been measured or tabulated, the values of these were taken directly from literature (**Supplementary Table 2**). Otherwise, the rate constants for these reactions were calculated assuming barrierless, diffusion-limited kinetics, using literature tabulated hydrated ionic radii and aqueous diffusion coefficients (**Supplementary Note 6 and Table 3**).

Kinetics in both directions are only slightly enhanced by the presence of the catalyst. The exact details of this catalytic enhancement are not evaluated in the present model. We note that more detailed models of dissociation could consider explicitly catalyst surface effects to resolve the nature of this enhancement.[4,59] However, we choose a more simple model for dissociation/recombination to improve computational efficiency (**Supplementary Note 2**). There is also a lack of rate parameters describing how the relevant mono- or multi- valent anions/cations interact with catalyst surfaces that frustrates attempts to invoke microkinetic modeling of these interfacial reactions. Furthermore, because this work is more focused on resolving mesoscale transport mechanisms for FB-BPMs, the exact details of the catalyst surface are not necessary to capture.

4.4 Mass and Charge Conservation in Forward-Bias Bipolar Membranes

Species conservation solves for the concentration of all relevant species,

$$\nabla \cdot \mathbf{N}_i = R_{B,i}, \tag{26}$$

where $\mathbf{N}_i$ is the flux of species i, and $R_{B,i}$ is a source term for the generation of species i from homogeneous reactions. The molar species flux is defined by the Nernst-Planck equation,

$$\mathbf{N_i} = -\frac{D_i c_i}{RT} \nabla \mu_i, \tag{27}$$

where D_i is the diffusivity of species i. Diffusivities for all species in aqueous electrolyte were taken from literature and reported in **Supplementary Table 1.** Within the membrane domains, diffusivities were corrected for the ionomer chemistry and morphology using the framework developed Grew et al.[63], discussed in greater detail in the Supplementary Methods **Section 2.** Membrane properties and geometry are reported in **Supplementary Table 5**.

The Poisson equation resolves the electrostatic potential and charge conservation in the domain,

$$-\frac{d^2\Phi}{dx^2} = \frac{F}{\varepsilon}\left(c_{\mathrm{M}}(x) + \sum_i z_i c_i \right), \tag{28}$$

where ε is the dielectric permittivity of the medium, defined to be that of water ($\varepsilon_{\mathrm{H_2O}}$) in the electrolyte domains. For the membrane domains, the dielectric permittivity (ε_{M}) is given by **Equation 14 in the Supplementary Methods**.

4.5 Boundary Conditions

Dirichlet boundary conditions set the concentrations of all modeled ionic species to their bulk electrolyte values within the AEL exchange solution (AEL-ES).

$$c_i\big|_{x=-\frac{L_{\mathrm{CL}}}{2}-L_{\mathrm{AEL}}-L_{\mathrm{AEL-ES}}} = c_{i,\mathrm{AEL-ES}}^{\mathrm{bulk}} \tag{29}$$

where the origin ($x = 0$) is defined at the center of the CL, L_{CL} is the CL thickness, L_{AEL} is the AEL thickness, and L_{AEL-ES} is the AEL-ES thickness. For all electrolytes studied, concentration BCs were set according to bulk pH measurements conducted by Dinh et al.[18] A table of concentration boundary conditions used for all electrolytes can be found in Supplementary **Table 4**.

The electrostatic potential is set to the measured membrane potential with another Dirichlet boundary condition,

$$\Phi\big|_{x=-\frac{L_{\mathrm{CL}}}{2}-L_{\mathrm{AEL}}-L_{\mathrm{AEL-ES}}} = -V_{\mathrm{app}} \tag{30}$$

where V_{app} is the total potential change across the modeled domain. The negative sign in (30) is by convention and ensures that FB is associated with positive current/voltage and RB is associated with negative current/voltage. At the end of the CEL-ES (rightmost boundary), Dirichlet boundary conditions are again employed to set species concentrations to their bulk values:

$$c_i\big|_{x=\frac{L_{\mathrm{CL}}}{2}+L_{\mathrm{CEL}}+L_{\mathrm{CEL-ES}}} = c_{i,\mathrm{CEL-ES}}^{\mathrm{bulk}} \tag{31}$$

where L_{CEL} is the CEL thickness, and $L_{\mathrm{CEL-ES}}$ is the CEL-ES thickness. Lastly, the electrostatic potential is set to a reference of 0 V at the CEL-ES boundary,

$$\Phi\big|_{x=\frac{L_{\mathrm{CL}}}{2}+L_{\mathrm{CEL}}+L_{\mathrm{CEL-ES}}} = 0\ \mathrm{V} \tag{32}$$

23

4.6 Model Fitting and Validation

Because the experiments from Dinh *et al.* simulated in this study employed Fumasep FBMs,[17,18] fitted parameters relating to the membrane diffusivity correction, CL thickness, and water-dissociation transfer coefficient were taken directly from prior work from our group that simulated Fumasep FBMs in reverse bias[27]. A fitted catalytic enhancement factor k_0 of 5× applied to the rate of dissociation/recombination within the CL domain was needed to ensure proper curvature of the FB polarization signature (**Supplementary Figure 2**). To validate these parameters, it is shown that the use of this single set of five parameters ($L_{\text{junction}}, L_{\text{BL}}, k_0, \alpha_{\text{WD}}, q$) (**See Supplementary Table 6**) is sufficient to reproduce the OCPs of all seventeen electrolytes tested by Dinh *et al.*[18] Sensitivity analysis **(Supplementary Note 7)** demonstrates that of these five parameters, only two of them (α_{WD}, and L_{junction}) affect the simulated OCP. Hence, only two adjustable parameters were fit a single time to reproduce the OCPs observed experimentally.

To reproduce the current-voltage behavior of the mixed KOH + KOAc|H2SO4 BPM studied by Toh *et al.*,[17] the AEL pK_b and selectivity of OH⁻ over OAc⁻ ($S_{\text{OH}}^{\text{OAc}}$) were introduced as additional parameters to capture the effects of fixed-charge neutralization and ion-selective partitioning, respectively. The pK_b was fitted to a value of 0.7 to match the polarization signature of the KOH|H2SO4 BPM and is consistent with the order of magnitude expected for anion-conducting polymers.[39] A single binary selectivity of 0.18 was then fitted to reproduce the attenuation of limiting current density and OCP with increasing OAc⁻ content in the electrolyte. This binary selectivity suggests that OAc⁻ is favored over OH⁻ in the AEL, which is consistent with literature reports of other AELs.[37] We note however, that CO2 uptake may influence the limiting current densities observed in the work of Toh *et al.*, which would affect the fitted $S_{\text{OH}}^{\text{OAc}}$ and $pK_{b,\text{AEL}}$; future work in CO2-free environments is required to deconvolute these effects fully. In total, a single set of seven parameters ($L_{\text{junction}}, L_{\text{BL}}, k_0, \alpha_{\text{WD}}, S_{\text{OH}}^{\text{OAc}}, pK_{b,\text{AEL}}, q$) are introduced in the model. Sensitivity analysis demonstrates that of the seven total parameters, only five of them (α_{WD}, L_{junction}, q, $pK_{b,\text{AEL}}$, and $S_{\text{OH}}^{\text{OAC}}$) affect the simulated j_{lim} and OCP **(Supplementary Note 7)**. Accordingly, a single set of these five adjustable parameters are needed to reproduce polarization behavior of BPMs exchanged with electrolytes of varying compositions and identities.

4.7 Computational Methods

Two customized General Partial Differential Equation (g) Modules, one representing mass conservation and one representing charge conservation, were solved simultaneously in COMSOL Multiphysics 6.0. The 1D continuum was discretized using a nonuniform mesh with heavy refinement near all interfaces and within the CL. The resulting mesh comprised 4224 elements. A mesh independence study confirmed results are independent of meshing for meshes containing greater than 4000 elements (**Supplementary Figure 3**). Achieving convergence in these asymmetric BPM systems was achieved by the following multistep initialization scheme. First, the Donnan equilibrium conditions were calculated analytically for a symmetric electrolyte system, and the initial values in each domain were set consistent with analytical Donnan calculation results. The model was then initialized with dissociation/recombination homogeneous source terms set to zero to obtain an initial solution consistent with the analytic calculation. Next, the pH of each electrolyte was parametrically swept to their desired values, and

the concentrations of the other species in each electrolyte were simultaneously modified using analytical equilibrium expressions that related their concentration to the parametrically swept bulk electrolyte pHs. Finally, the homogeneous reaction source terms were turned on *via* logarithmic parametric sweeps. This initialization scheme was run for each class of electrolyte (monovalent cation, monovalent anion, divalent anion, trivalent anion, mixed electrolyte). All simulations were run using the Multifrontal Massively Parallel sparse direct Solver (MUMPS) employing Newton's Method with a tolerance of 0.001 and a recovery damping factor of 0.75.

Acknowledgments

Author Contributions

J.C.B. conceived of the study, developed the continuum model and theory, and collected and analyzed simulation data. A.K.L. performed initial model validations. E.W.L., P.G., and F.G. assisted with theory development and provided modeling support. W.L.T. provided experimental data and assisted with data interpretation. J.C.B and E.W.L. prepared the initial draft of the manuscript. A.Z.W., A.T.B, and Y.S. supervised the project and assisted with data analysis and interpretation. All authors engaged in the writing and revision of the manuscript.

Ethics Declarations

Competing Interests

The authors declare no competing interests.

Data Availability Statement

All data associated with the figures in this paper can be found in the Supplementary Data.

References

1. Pärnamäe, R. *et al.* Bipolar membranes: A review on principles, latest developments, and applications. *J. Memb. Sci.* **617**, (2021).

2. Blommaert, M. A. *et al.* Insights and Challenges for Applying Bipolar Membranes in Advanced Electrochemical Energy Systems. *ACS Energy Lett.* **6**, 2539–2548 (2021).

3. Bui, J. C. *et al.* Multi-scale physics of bipolar membranes in electrochemical processes. *Nat. Chem. Eng.* **1**, 45–60 (2024).

4. Lucas, É. *et al.* Asymmetric Bipolar Membrane for High Current Density Electrodialysis Operation with Exceptional Stability. *Chemrxiv* 1–33 (2023). doi:10.26434/chemrxiv-2023-n4c6x

5. Oener, S. Z., Foster, M. J. & Boettcher, S. W. Accelerating water dissociation in bipolar membranes and for electrocatalysis. *Science (80-.).* **369**, 1099–1103 (2020).

6. Li, Y. *et al.* Bipolar Membrane Electrodialysis for Ammonia Recovery from Synthetic Urine: Experiments, Modeling, and Performance Analysis. *Environ. Sci. Technol.* **55**, 14886–14896 (2021).

7. Dong, H., Laguna, C. M., Liu, M. J., Guo, J. & Tarpeh, W. A. Electrified Ion Exchange Enabled by Water Dissociation in Bipolar Membranes for Nitrogen Recovery from Source-Separated Urine. *Environ. Sci. Technol.* **56**, 16134–16143 (2022).

8. van Linden, N., Bandinu, G. L., Vermaas, D. A., Spanjers, H. & van Lier, J. B. Bipolar membrane electrodialysis for energetically competitive ammonium removal and dissolved ammonia production. *J. Clean. Prod.* **259**, 120788 (2020).

9. Bui, J. C. *et al.* Analysis of bipolar membranes for electrochemical capture from air and oceanwater. *Energy Environ. Sci.* **Advance Ar**, (2023).

10. Eisaman, M. D. *et al.* CO2 separation using bipolar membrane electrodialysis. *Energy Environ. Sci.* **4**, 1319–1328 (2011).

11. Iizuka, A. *et al.* A Process for Capturing CO2 from the Atmosphere. *Ind. Eng. Chem. Res.* **4**, 1–11 (2022).

12. Luo, J. *et al.* Bipolar Membrane-Assisted Solar Water Splitting in Optimal pH. *Adv. Energy Mater.* **6**, 1–7 (2016).

13. Marin, D. H. *et al.* Hydrogen production with seawater-resilient bipolar membrane electrolyzers. *Joule* **7**, 765–781 (2023).

14. Lees, E. W. *et al.* Electrolytic Methane Production from Reactive Carbon Solutions. *ACS Energy Lett.* **7**, 1712–1718 (2022).

15. Li, Y. C. *et al.* Bipolar Membranes Inhibit Product Crossover in CO2 Electrolysis Cells. *Adv. Sustain. Syst.* **2**, 1–5 (2018).

16. Xie, K. *et al.* Bipolar membrane electrolyzers enable high single-pass CO2 electroreduction to multicarbon products. *Nat. Commun.* **13**, 1–12 (2022).

17. Toh, W. L., Dinh, H. Q., Chu, A. T., Sauvé, E. R. & Surendranath, Y. The role of ionic blockades in controlling the efficiency of energy recovery in forward bias bipolar membranes. *Nat. Energy* **8**, 1405–1416 (2023).

18. Dinh, H. Q., Toh, W. L., Chu, A. T. & Surendranath, Y. Neutralization Short-Circuiting with Weak Electrolytes Erodes the Efficiency of Bipolar Membranes. *ACS Appl. Mater. Interfaces* **15**, 4001–4010 (2023).

19. Gabrielsson, E. O., Tybrandt, K. & Berggren, M. Ion diode logics for pH control. *Lab Chip* **12**, 2507–2513 (2012).

20. Blommaert, M. A. *et al.* Orientation of a bipolar membrane determines the dominant ion and carbonic species transport in membrane electrode assemblies for CO2reduction. *J. Mater. Chem. A* **9**, 11179–11186 (2021).

21. Peng, S. *et al.* A self-humidifying acidic-alkaline bipolar membrane fuel cell. *J. Power Sources* **299**, 273–279 (2015).

22. Mitchell, J. B., Chen, L., Langworthy, K., Fabrizio, K. & Boettcher, S. W. Catalytic Proton-Hydroxide Recombination for Forward-Bias Bipolar Membranes. *ACS Energy Lett.* **7**, 3967–3973 (2022).

23. Yan, Z. *et al.* High-Voltage Aqueous Redox Flow Batteries Enabled by Catalyzed Water Dissociation and Acid-Base Neutralization in Bipolar Membranes. *ACS Cent. Sci.* **7**, 1028–1035 (2021).

24. Chen, R. Redox flow batteries: Mitigating cross-contamination via bipolar redox-active materials and bipolar membranes. *Curr. Opin. Electrochem.* **37**, 101188 (2023).

25. Xi, D. *et al.* Mild pH-decoupling aqueous flow battery with practical pH recovery. *Nat. Energy* (2024). doi:10.1038/s41560-024-01474-1

26. Lucas, É., Han, L., Sullivan, I., Atwater, H. A. & Xiang, C. Measurement of ion transport properties in ion exchange membranes for photoelectrochemical water splitting. *Front. Energy Res.* **10**, 1–11 (2022).

27. Bui, J. C., Digdaya, I., Xiang, C., Bell, A. T. & Weber, A. Z. Understanding Multi-Ion Transport Mechanisms in Bipolar Membranes. *ACS Appl. Mater. Interfaces* **12**, 52509–52526 (2020).

28. Newman, J. & Thomas-Alyea, K. E. *Electrochemical Systems*. (John Wiley and Sons, Inc., 2004).

29. Pärnamäe, R. *et al.* Origin of Limiting and Overlimiting Currents in Bipolar Membranes. *Environ. Sci. Technol.* **57**, 9664–9674 (2023).

30. Crandall, B. S., Overa, S., Shin, H. & Jiao, F. Turning Carbon Dioxide into Sustainable Food and Chemicals: How Electrosynthesized Acetate Is Paving the Way for Fermentation Innovation. *Acc. Chem. Res.* **56**, 1505–1516 (2023).

31. Ramdin, M. *et al.* High Pressure Electrochemical Reduction of CO2 to Formic Acid/Formate: A Comparison between Bipolar Membranes and Cation Exchange Membranes. *Ind Eng Chem Res* **58**, 1834–1847 (2019).

32. Rabinowitz, J. A. & Kanan, M. W. The future of low-temperature carbon dioxide electrolysis depends on solving one basic problem. *Nat. Commun.* 10–12 (2020). doi:10.1038/s41467-020-19135-8

33. Peng, J., Roy, A. L., Greenbaum, S. G. & Zawodzinski, T. A. Effect of CO2 absorption on ion and water mobility in an anion exchange membrane. *J. Power Sources* **380**, 64–75 (2018).

34. Lees, E. W., Bui, J. C., Song, D., Weber, A. Z. & Berlinguette, C. P. Continuum Model to Define the Chemistry and Mass Transfer in a Bicarbonate Electrolyzer. *ACS Energy Lett.* **7**, 834–842 (2022).

35. Jouny, M., Luc, W. & Jiao, F. High-rate electroreduction of carbon monoxide to multi-carbon products. *Nat. Catal.* **1**, 748–755 (2018).

36. Li, T., Lees, E. W., Zhang, Z. & Berlinguette, C. P. Conversion of Bicarbonate to Formate in an Electrochemical Flow Reactor. *ACS Energy Lett.* **5**, 2624–2630 (2020).

37. Wheaton, R. M. & Bauman, W. C. Properties of Strongly Basic Anion Exchange Resins. *Ind. Eng. Chem.* **43**, 1088–1093 (1951).

38. Crothers, A. R., Darling, R. M., Kushner, D. I., Perry, M. L. & Weber, A. Z. Theory of Multicomponent Phenomena in Cation-Exchange Membranes: Part III. Transport in Vanadium Redox-Flow-Battery Separators. *J. Electrochem. Soc.* **167**, (2020).

39. Ramaswamy, N. & Mukerjee, S. Alkaline Anion-Exchange Membrane Fuel Cells: Challenges in Electrocatalysis and Interfacial Charge Transfer. *Chem. Rev.* **119**, 11945–11979 (2019).

40. Andersen, M. B. *et al.* Current-induced membrane discharge. *Phys. Rev. Lett.* **109**, 1–5 (2012).

41. Krewer, U., Weinzierl, C., Ziv, N. & Dekel, D. R. Impact of carbonation processes in anion exchange membrane fuel cells. *Electrochim. Acta* **263**, 433–446 (2018).

42. Suzuki, S., Muroyama, H., Matsui, T. & Eguchi, K. Influence of CO2 dissolution into anion exchange membrane on fuel cell performance. *Electrochim. Acta* **88**, 552–558 (2013).

43. She, X. *et al.* Pure-water-fed, electrocatalytic CO2 reduction to ethylene beyond 1,000 h stability at 10 A. *Nat. Energy* **9**, 81–91 (2024).

44. Fischer, R., Dessiex, M. A., Marone, F. & Buchi, F. N. Gas-Induced Structural Damages in Forward-Bias Bipolar Membrane CO2 Electrolysis Studied by Fast X-ray Tomography. *ACS Appl. Energy Mater.* **Advance Ar**, (2024).

45. Gerhardt, M. R. *et al.* Methods—Practices and Pitfalls in Voltage Breakdown Analysis of Electrochemical Energy-Conversion Systems. *J. Electrochem. Soc.* (2021). doi:10.1149/1945-7111/abf061

46. Pärnamäe, R. *et al.* The acid–base flow battery: Sustainable energy storage via reversible water dissociation with bipolar membranes. *Membranes (Basel).* **10**, 1–20 (2020).

47. Yan, H. *et al.* Bipolar membrane-assisted reverse electrodialysis for high power density energy conversion via acid-base neutralization. *J. Memb. Sci.* **647**, 120288 (2022).

48. Kitto, D. & Kamcev, J. The need for ion-exchange membranes with high charge densities. *J. Memb. Sci.* **677**, 121608 (2023).

49. Kusoglu, A. & Weber, A. Z. New Insights into Perfluorinated Sulfonic-Acid Ionomers. *Chem. Rev.* **117**, 987–1104 (2017).

50. Kushner, D. I., Crothers, A. R., Kusoglu, A. & Weber, A. Z. Transport phenomena in flow battery ion-conducting membranes. *Curr. Opin. Electrochem.* **21**, 132–139 (2020).

51. Bui, J. C. *et al.* Engineering Catalyst − Electrolyte Microenvironments to Optimize the Activity and Selectivity for the Electrochemical Reduction of CO2on Cu and Ag. *Acc. Chem. Res.* **55**, 484–494 (2022).

52. Tricker, A. W. *et al.* Engineering Bipolar Interfaces for Water Electrolysis Using Earth-Abundant Anodes. *ACS Energy Lett.* **8**, 5275–5280 (2023).

53. Heßelmann, M. *et al.* Pure-Water-Fed Forward-Bias Bipolar Membrane CO 2 Electrolyzer. *ACS Appl. Mater. Interfaces* (2024). doi:10.1021/acsami.4c02799

54. Wei Lun Toh,‡ Hieu Q. Dinh,‡ An T. Chu, Ethan, R. Sauvé, Y. S. Ionic Blockades Control the Efficiency of Energy Recovery in Forward Bias Bipolar Membranes. *Chemrxiv* 1–14 (2023).

55. Craig, N. P. Electrochemical Behavior of Bipolar Membranes. (2013).

56. Onsager, L. & Fuoss, R. M. Irreversible processes in electrolytes. Diffusion, conductance, and viscous flow in arbitrary mixtures of strong electrolytes. *J. Phys. Chem.* **36**, 2689–2778 (1932).

57. Onsager, L. Deviations from Ohm ′ s Law in Weak. *J. Chem. Phys.* **2**, 599–615 (1934).

58. Kaiser, V., Bramwell, S. T., Holdsworth, P. C. W. & Moessner, R. Onsager's Wien Effect on a Lattice. *Nat. Mater.* **12**, 1033–1037 (2013).

59. Bui, J. C., Corpus, K. R. M., Bell, A. T. & Weber, A. Z. On the Nature of Field Enhanced Water Dissociation in Bipolar Membranes. *J. Phys. Chem. C* **125**, 24974–24987 (2021).

60. Lin, M., Digdaya, I. A. & Xiang, C. Modeling the electrochemical behavior and interfacial junction profiles of bipolar membranes at solar flux relevant operating current densities. *Sustain. Energy Fuels* **5**, 2149–2158 (2021).

61. Onsager, L. Deviations from Ohm's Law in Weak. *J. Chem. Phys.* **2**, 599–615 (1934).

62. Ramírez, P., Rapp, H. J., Reichle, S., Strathmann, H. & Mafé, S. Current-voltage curves of bipolar membranes. *J. Appl. Phys.* **72**, 259–264 (1992).

63. Grew, K. N. & Chiu, W. K. S. A Dusty Fluid Model for Predicting Hydroxyl Anion Conductivity in Alkaline Anion Exchange Membranes. *J. Electrochem. Soc.* **157**, B327 (2010).